

Does the HCN/CO ratio trace the star-forming fraction of gas? I. A comparison with analytical models of star formation.

ASHLEY R. BEMIS ^{1,2} AND CHRISTINE D. WILSON ²

¹*Leiden Observatory, Leiden University, PO Box 9513, 2300 RA Leiden, The Netherlands*

²*McMaster University, 1280 Main St W, Hamilton ON L8S 4M1, Canada*

ABSTRACT

We use archival ALMA observations of the HCN and CO $J = 1 - 0$ transitions, in addition to the radio continuum at 93 GHz, to assess the relationship between dense gas, star formation, and gas dynamics in ten, nearby (U)LIRGs and late-type galaxy centers. We frame our results in the context of turbulent and gravoturbulent models of star formation to assess if the HCN/CO ratio tracks the gravitationally-bound, star-forming gas in molecular clouds (f_{grav}) at sub-kpc scales in nearby galaxies. We confirm that the HCN/CO ratio is a tracer of gas above $n_{\text{SF}} \approx 10^{4.5} \text{ cm}^{-3}$, but the sub-kpc variations in HCN/CO do not universally track f_{grav} . We find strong evidence for the use of varying star formation density threshold models, which are able to reproduce trends observed in t_{dep} and ϵ_{ff} that fixed threshold models cannot. Composite lognormal and powerlaw models outperform pure lognormal models in reproducing the observed trends, even when using a fixed powerlaw slope. The ability of the composite models to better reproduce star formation properties of the gas provides additional indirect evidence that the star formation efficiency per free-fall time is proportional to the fraction of gravitationally-bound gas.

Keywords: dense gas — star formation — galaxies — turbulence — star formation models

1. INTRODUCTION

A current challenge for understanding star formation in molecular clouds is determining the fraction of gas that is converted into stars over a cloud’s lifetime. Observations show that sites of star formation are primarily in regions of dense molecular gas in Milky Way clouds (Lada et al. 1991a,b; Helfer & Blitz 1997a,b), and these regions are confined to ~ 0.1 pc scales within larger molecular structures in the form of clumps or filaments (André et al. 2016). Within these structures of gas, it is the fraction of gravitationally-bound gas that goes on to form stars. Analytical models of star formation rely on estimates of the self-gravitating gas fraction, f_{grav} , to then predict the star formation rate (SFR, e.g. Krumholz & McKee 2005; Hennebelle & Chabrier 2011; Padoan & Nordlund 2011; Federrath & Klessen 2012; Burkhardt & Mocz 2019), which makes f_{grav} an important parameter to constrain observationally.

Extragalactic observations rely on molecular transitions with high critical densities, $n_{\text{crit}} \gtrsim 10^4 \text{ cm}^{-3}$ to gain information on the dense gas in other galaxies. The most commonly-used dense molecular gas tracer in extragalactic studies is the HCN $J = 1 - 0$ transition (Gao & Solomon 2004a,b). Under the common assumption that the total emissivity of HCN traces the dense gas mass, $I_{\text{HCN}} \propto \Sigma_{\text{dense}}$, then the ratio of the HCN and CO emissivities, $I_{\text{HCN}}/I_{\text{CO}}$, is proportional to the fraction of molecular gas in the dense phase, f_{dense} . If the dense gas mass traced by HCN is also self-gravitating, then this line ratio is a simple, observational method for estimating f_{grav} . However, the Interstellar Medium (ISM) of galaxies resides at a range of densities $\lesssim 1 - \gg 10^8 \text{ cm}^{-3}$, and molecular transitions are sensitive to a continuum of these densities, including some fraction below their critical density (Shirley 2015; Leroy et al. 2017a). Recent studies within the Milky Way have also shown that HCN may predominantly trace moderate gas densities (Kauffmann et al. 2017), rather than denser gas associated with star formation. The fraction of ”CO-dark” or ”CO-faint” gas may also contribute to variations in $I_{\text{HCN}}/I_{\text{CO}}$ (Grenier et al. 2005; Wolfire et al. 2010; Bolatto et al. 2013). On average in the Milky

Way, $\sim 30\%$ of molecular Hydrogen appears to be "CO-faint" (Pineda et al. 2013; Langer et al. 2014). This fraction is higher in lower-metallicity gas (Pineda et al. 2013; Jameson et al. 2018; Chevance et al. 2020) and appears to be more significant for clouds at lower masses (Grenier et al. 2005; Bolatto et al. 2013) and at higher radii in the Milky Way (Pineda et al. 2013; Langer et al. 2014; Chevance et al. 2020). This would likely result in overestimates of f_{dense} in lower mass clouds, assuming HCN emission is not affected in the same way. This is likely less significant in more extreme systems (such as U/LIRGs) or galaxy centers, such as those studied in this paper.

The dynamics of the gas in the ISM are set by a combination of gravity, turbulence, and magnetic fields, and these processes act together to set the spatial structure of gas in ISM clouds. These processes also likely play a role in setting the star formation properties of the ISM. One type of analytical model, gravoturbulent models of star formation, aims to predict both the observed structure of gas clouds and their star formation properties. In particular, gravoturbulent models of star formation predict the shape of the gas volume density Probability Distribution Function (n -PDF) and the star formation efficiency (ϵ_{ff}) over a free-fall time (t_{ff})¹ (Krumholz & McKee 2005; Padoan & Nordlund 2011; Hennebelle & Chabrier 2011; Federrath & Klessen 2012; Burkhardt 2018; Imara & Burkhardt 2016).² Studies have found that the *column* density PDF of the diffuse ($n < 1 \text{ cm}^{-3}$) component of gas in the Milky Way and M33 is consistent with a lognormal PDF (cf. Berkhuijsen & Fletcher 2008; Hill et al. 2008; Tabatabaei et al. 2008; Burkhardt et al. 2015). The seminal analytical work by Vazquez-Semadeni (1994) showed that if the turbulent ISM develops a series of isothermal and interacting supersonic shocks, the gas would naturally follow a lognormal PDF (cf. Vazquez-Semadeni 1994; Padoan et al. 1997; Scalo et al. 1998; Nordlund & Padoan 1999. In this picture, the shocks amplify each other via a turbulent cascade of energy, and this multiplicative process results in the gas density PDF taking on a lognormal shape (cf. Vazquez-Semadeni 1994; Padoan et al. 1997; Scalo et al. 1998; Nordlund & Padoan 1999; Chen et al. 2018).

¹ Brunt et al. (2010) find that the two-dimensional column density distribution is a compressed version of the three-dimensional (volume) density distribution. Burkhardt & Lazarian (2012) provide an analytical framework for connecting these two distributions in the case that both contain lognormal components, which we adopt in this paper.

² Free-fall time is treated differently depending on the framework used, and in reality it must be a reflection of multiple free-fall times from the array of gas densities that span the n -PDF.

Observations of molecular regions of the ISM reveal that the gas *column* density PDF takes on a different form at high densities. The highest-density regions within more-evolved molecular clouds contribute a powerlaw tail to the gas column density PDF (cf. Chen et al. 2018), with some cloud PDFs being almost entirely powerlaw (e.g. Kainulainen et al. 2009; Schneider et al. 2013; Lombardi et al. 2015; Schneider et al. 2015, 2016; Alves et al. 2017). This powerlaw has also been observed in simulations that develop self-gravitating gas (cf. Ballesteros-Paredes et al. 2011; Collins et al. 2012; Schneider et al. 2015; Burkhardt et al. 2017; Padoan et al. 2017. These results strongly suggest that the gas density PDF in a star-forming molecular cloud is likely a combination of a lognormal and powerlaw shape, and that the powerlaw tail is potentially the result of gas becoming self-gravitating. The fraction of gas within this powerlaw tail would then be the self-gravitating gas fraction, f_{grav} . The density at which the n -PDF transitions from a lognormal to powerlaw shape would then represent when gas becomes available to star formation, n_{SF} . The fraction of dense gas mass above n_{SF} (f_{grav}), relative to the total mass of a star-forming cloud is then:

$$f_{\text{grav}} = \frac{M(n > n_{\text{SF}})}{M} \quad (1)$$

Turbulent models of star formation estimate ϵ_{ff} by integrating over a purely lognormal gas density PDF, also above a gas threshold density (cf. Krumholz & McKee 2005; Hennebelle & Chabrier 2011; Padoan & Nordlund 2011; Federrath & Klessen 2012). This threshold density is also meant to capture when gas becomes self-gravitating in the ISM, so that the fraction of gas above this threshold is f_{grav} in these models. However, lognormal-only models fail to explain observed variations in ϵ_{ff} and mach number, \mathcal{M} , seen in some galaxies (e.g. Leroy et al. 2017b). For example, Giant Molecular Clouds (GMCs) in M51 show a weak anti-correlation between velocity dispersion (which is proportional to \mathcal{M} , see Eq. 11) and the star formation efficiency of gas per free-fall time, ϵ_{ff} .³ Leroy et al. (2017a) argue that this anti-correlation may reflect differences in the dynamical state of their clouds with galactocentric radius.

Burkhardt & Mocz (2019) show that including a powerlaw tail in the gas volume density PDF reproduces the observed variations in ϵ_{ff} in M51, without requiring changes in the dynamical state of the clouds and without explicitly setting n_{SF} . They find a slight anti-correlation

³ We briefly discuss the observational uncertainties associated with estimates of \mathcal{M} , which depend on measurements of velocity dispersion, in §2.5.

between ϵ_{ff} and \mathcal{M} for virialized clouds ($\alpha_{\text{vir}} \approx 1$). This anti-correlation coincides with an increasing depletion time with \mathcal{M} , in agreement with the findings from PAWS (Leroy et al. 2017b). $\epsilon_{\text{ff}} \propto f_{\text{grav}}$ implies f_{grav} may also anticorrelate with \mathcal{M} . Thus, without needing to explicitly set n_{SF} , it is ultimately a decrease in f_{grav} with respect to increasing \mathcal{M} that leads to the anti-correlation between σ_{rv} and ϵ_{ff} (Burkhart & Mocz 2019). However, in starbursts where \mathcal{M} is higher, we see higher ϵ_{ff} , and shorter t_{dep} , on average (Wilson et al. 2019). Starbursts typically have enhanced HCN/CO ratios in addition to shorter depletion time, t_{dep} (Kennicutt & De Los Reyes 2021). If $I_{\text{HCN}}/I_{\text{CO}} \propto f_{\text{dense}}$ and $f_{\text{dense}} \propto f_{\text{grav}}$, then the result from BM19 appears contrary to what is observed in starbursts.

A potential explanation for these differences may be differences in the timescale for star formation, which may be set by the environment that a gas cloud is immersed in. The star formation law can be written as (Krumholz et al. 2012):

$$t_{\text{ff}} \Sigma_{\text{SFR}} = \epsilon_{\text{ff}} \Sigma_{\text{gas}} \quad (2)$$

where Σ_{gas} is the gas surface density, Σ_{SFR} is the star formation rate surface density, and t_{ff} is the free-fall time and is set by the self-gravity of a cloud.

Burkhart & Mocz (2019) demonstrate the connection between f_{grav} and the instantaneous efficiency of the gas, $\epsilon_{\text{inst}} \approx \epsilon_0 f_{\text{grav}}$, that reflects both the local efficiency, ϵ_0 (set by e.g. stellar feedback), and f_{grav} . This local efficiency may correlate with its observational analog, the star formation efficiency per free-fall time, ϵ_{ff} (Krumholz & McKee 2005; Lee et al. 2016). Furthermore, if turbulence plays a significant role in setting n_{SF} , then we may find a correlation between ϵ_{ff} and observed velocity dispersions of gas, and turbulent pressure. Turbulent models of the ISM predict a dependence of σ_{n/n_0} , the density variance of the volume density PDF (n -PDF) on the sonic mach number, $\mathcal{M} = \sigma_{v,3D}/c_s$ ⁴, within individual star-forming clouds. Lada et al. (1994) found a correlation between the extinction, A_V , in the Dark Cloud IC 5126 and the standard deviation of A_V , with extinction increasing with dispersion (Goodman et al. 2009). Kainulainen & Tan (2013) find a correlation between measurements of the velocity dispersion from ¹²CO and ¹³CO and the density contrast (N/N_0) of column density PDFs (N -PDFs) derived from IR data in

several Milky Way clouds. Combined, these correlations imply that the CO velocity dispersion may be sensitive to the density variance of the N -PDF, σ_{N/N_0} (where $\sigma_{N/N_0} \propto \ln(N/N_0)$), and therefore a probe of the ISM physics.

In external galaxies where resolution is limited, molecular line ratios are an additional tool for assessing n -PDF shape. Shirley (2015) showed that molecular transitions have an emissivity⁵ that extends over a range of gas densities, including a significant amount of emission at densities below the critical density associated with that transition⁶. To determine if molecular line ratios stay sensitive to n -PDF shape, Leroy et al. (2017a) model molecular line emissivities and explore a range of n -PDF shapes. They find that dense gas tracers (such as HCN and HCO⁺) are more sensitive to changes in the shape of the n -PDF than lower-density tracers like CO. Combining molecular line ratios of dense gas tracers with information on kinematics is therefore a promising tool for assessing n -PDF information of clouds in external galaxies.

To assess the relationship between the HCN/CO ratio and f_{grav} , we look to more extreme star-forming environments in which turbulence is stronger (e.g. mergers, starbursts, (U)LIRGs, barred galaxies). We study a sample of 10 (U)LIRGs and disk galaxy centers that have archival CO, HCN, CN, and HCO⁺ $J = 1 - 0$ data, in addition to 93 GHz radio continuum. In this paper, we focus on general trends of the HCN/CO ratio, the star formation rate surface density, and ϵ_{ff} , and we compare these modelled trends with the observed trends in our sample. We use the EMPIRE sample of galaxies (Jiménez-Donaire et al. 2019) as a comparison, which predominantly targets normal regions of star formation within galaxy disks.

2. DATA AND SAMPLE

Our sample consists of ten nearby ($z < 0.03$) galaxies, including the dense centers of five disk galaxies and five mergers and (U)LIRGs. We list these galaxies and their basic properties in Table 1. Four of the five disk galaxies in our sample are also barred. For each galaxy, we image archival ALMA data of the HCN, CN, CO, and HCO⁺ $J = 1 - 0$ transitions, in addition to the radio continuum emission at 93 GHz. The data are uv -matched and tapered to a common beam for each individual galaxy.

⁴ The sound speed is given by $c_s = \sqrt{kT_{\text{kin}}/\mu m_{\text{H}}}$, T_{kin} is the gas kinetic temperature, $\mu = 2.33$ (Kauffmann et al. 2008) is the mean molecular weight, and m_{H} is the Hydrogen mass. $\sigma_{v,3D}$ is the three-dimensional velocity dispersion and is related to the one-dimensional velocity dispersion via $\sigma_{3D,v} = \sqrt{3}\sigma_v$.

⁵ Emissivity, which describes the emission per mass surface density, is effectively the inverse of a molecular line conversion factor.

⁶ Here the critical density is the density at which collisional interactions balance instantaneous de-excitation of a particular molecular transition (Draine 2010)

The sample selection and data reduction process are presented in [Wilson et al. \(submitted\)](#) in detail, except for NGC 4038/9, NGC 1808, and NGC 3351, which have been reduced and imaged separately at higher velocity resolutions to be included in this analysis.

2.1. Moment Maps

We produce maps of integrated intensity and velocity dispersion of the CO and HCN $J = 1 - 0$ transitions using the Astropy Spectral Cube package ([Ginsburg et al. 2019](#)). We implement a masking method similar to that in [Sun et al. \(2018\)](#) and summarize the masking method here:

1. The r.m.s. noise is estimated in each channel of each datacube using Median Absolute Standard Deviation.
2. Peaks of emission with a signal-to-noise ratio (SNR) of at least five across two channels are identified within each datacube.
3. Masks are expanded around these peaks down to channels with emission at a SNR of three.
4. Emission from regions smaller than a beam area are masked.

We calculate the uncertainty in integrated intensity and velocity dispersion using Eqs. [A2](#) and [A6](#), respectively. We require that all pixels have $\text{SNR} > 3$ in integrated intensity in addition to a $\text{SNR} > 2$ in velocity dispersion.

2.2. Molecular Gas Surface Densities

One of the main goals of this study is to assess variations in the fraction of gas in the dense phase as traced by the HCN and CO molecular line luminosities. Our analysis allows us to estimate trends in the HCN and CO luminosity-to-mass conversion factors (cf. [Bolatto et al. 2013](#)), which we define as:

$$\alpha_{\text{mol}} = \frac{\Sigma_{\text{mol}}}{I_{\text{mol}}} \quad [\text{M}_{\odot} \text{pc}^2 (\text{K km s}^{-1})^{-1}] \quad (3)$$

where Σ_{mol} is the mass surface density of the molecular gas, including Helium, $I_{\text{mol}} = L_{\text{mol}}/A_{\text{pix}}$ is the intensity in units of K km s^{-1} , and L_{mol} is total luminosity over the physical area of a pixel, A_{pix} . To calculate the molecular gas mass surface density, Σ_{mol} , we use:

$$\Sigma_{\text{mol}} = \alpha_{\text{mol}} I_{\text{mol}} \cos(i). \quad (4)$$

We apply inclination angles only to the disk galaxies in this sample, as inclination angles are typically uncertain in mergers and (U)LIRGs. Thus, the uncorrected

measurements of galaxies with non-zero inclinations will result in overestimates of Σ_{mol} and other surface densities.

For ease of comparison with other studies our fiducial value is $\alpha_{\text{CO}} = 1.1 [\text{M}_{\odot} (\text{K km s}^{-1} \text{pc}^2)^{-1}]$ for our sample of galaxies, the (U)LIRG value including Helium ([Downes et al. 1993](#)), which is ~ 4 times lower than the Milky Way value. This lower value is motivated by evidence that gas in these systems is subject to more extreme excitation mechanisms, e.g. higher temperatures and densities (cf. [Bolatto et al. 2013](#); [Downes et al. 1993](#) and references therein). Additionally, the gas traced by CO in these systems often shows broad line widths, potentially reducing the opacity of the CO transition ([Bolatto et al. 2013](#); [Downes et al. 1993](#)). [Downes et al. \(1993\)](#) also suggest that CO may be subthermally excited ($T_{\text{ex}} < T_{\text{kin}}$) in starbursts and (U)LIRGs. We choose a fixed value of $\alpha_{\text{CO}} = 4.35 [\text{M}_{\odot} (\text{K km s}^{-1} \text{pc}^2)^{-1}]$ for the EMPIRE sample of galaxies, since these are mostly disk galaxies and are likely more similar to the Milky Way than to starbursts. Since we already have NGC 3627 in our sample, we drop NGC 3627 from the EMPIRE data.

The HCN conversion factor is less certain. Historically, $\alpha_{\text{HCN}} \approx 13.6 [\text{M}_{\odot} (\text{K km s}^{-1} \text{pc}^2)^{-1}]$ has been used ([Gao & Solomon 2004a,b](#)), which is appropriate for a virialized cloud core with a mean density $n_{\text{H}_2} \sim 3 \times 10^4 \text{cm}^{-3}$ and brightness temperature $T_{\text{B}} \sim 35 \text{K}$ (e.g., [Radford et al. 1991](#), including Helium). This HCN conversion factor assumes that this molecular transition is optically thick, and that the gas it traces is in local thermodynamic equilibrium (LTE). In [Bemis \(2020\)](#) and [Bemis & Wilson, in prep.](#) we explore variations in the relative values of α_{HCN} and α_{CO} using a non-LTE radiative transfer analysis. If all of the above assumptions are true, then the fraction of dense gas traced by HCN/CO is given by:

$$f_{\text{dense}} = \frac{\alpha_{\text{HCN}} I_{\text{HCN}}}{\alpha_{\text{CO}} I_{\text{CO}}}. \quad (5)$$

with $\alpha_{\text{HCN}}/\alpha_{\text{CO}} = 3.2$ implied from the above discussion. We do this assuming that the physical effects impacting α_{CO} will impact α_{HCN} in a similar way. Simulations show that a slight reduction in α_{HCN} does happen in presence of higher gas temperatures ($T_{\text{kin}} = 20 \text{K}$, cf. [Onus et al. 2018](#)), similar to our expectation for α_{CO} . Furthermore, by using $\alpha_{\text{HCN}}/\alpha_{\text{CO}} = 3.2$ our plots of f_{dense} are a direct reflection of the HCN/CO ratio. We distinguish this calculation of f_{dense} from analytical estimates of the fraction of dense, star-forming gas which is generally defined as the mass fraction above the density at which gas becomes self-gravitating, f_{grav} .

Table 1. Spatial and spectral resolutions of the data for each galaxy.

Galaxy	Beam (")	Distance ^a (Mpc)	Scale (pc/beam)	δv (km s ⁻¹)	i^b (°)	z	AGN	Bar	Interacting	Classification
M83	2.10	4.7	48	10	24	0.00171	–	Y	–	SB
Circinus	3.00	4.2	61	20	66	0.00145	Sy 2	–	–	SB
NGC 3351	3.45	9.3	156	10	45.1	0.00260	–	Y	N	SB
NGC 3627	4.15	9.4	189	20	56.5	0.00243	LINER/Sy 2	Y	Y	Post-SB
NGC 1808	3.75	7.8	142	10	57	0.00322	Sy 2	Y	–	SB
NGC 7469	0.95	66.4	306	20	45	0.01632	Sy 1	–	Y	LIRG
NGC 3256	2.20	44	469	27.5	–	0.00935	South Nucleus	N	Y	LIRG
NGC 4038	5.00	22	110	5.2	–	0.00569	–	N	Y	SB
IRAS 13120-5453	1.10	134	715	20	–	0.02076	Sy 2	N	–	ULIRG
VV114	2.30	81	903	20	–	0.02007	East Nucleus	N	Y	LIRG

^a Distances from [Wilson et al. \(submitted\)](#)

^b M83: [Tilanus & Allen \(1993\)](#); Circinus: [Jarrett et al. \(2003\)](#); NGC 3351 & NGC 3627: [Sun et al. \(2020\)](#); NGC 1808: [Salak et al. \(2019\)](#)

* Distances and redshifts are also listed, which are used to determine the physical scale (in pc) per pixel, and to convert measured flux to luminosities. Redshifts are taken from the NASA/IPAC Extragalactic Database (NED). Inclination angles are taken from the papers listed below the table. Distances are the same as in [Wilson et al. \(submitted\)](#), except for NGC 3627. We use the distance for NGC 3627 taken from [Jiménez-Donaire et al. \(2019\)](#) for consistency when comparing with the EMPIRE data. We also list the presence/absence of an AGN, bar, or interaction with another galaxy. These classifications are taken from NED.

2.3. The Radio Continuum SFR

We detect radio continuum emission at 93 GHz in all of our sources and use this as our SFR tracer. The radio continuum is a combination of thermal (T) free-free emission and non-thermal (NT) synchrotron emission from regions with massive star formation, spanning $\sim 1 - 100$ GHz. At 93 GHz, we are in the regime where thermal free-free emission from young star-forming regions will likely dominate the radio continuum emission. Non-thermal emission is expected to contribute $\sim 25\%$ to the radio continuum luminosity at this frequency (see [Wilson et al. 2019; Murphy et al. 2011](#)), assuming an electron temperature $T_e \sim 10^4$ K and non-thermal spectral index $\alpha_{\text{NT}} \sim 0.84$. This fraction will change if there are variations in either T_e or α_{NT} . We adopt fixed values for $\alpha_{\text{NT}} = 0.84$ and $T_e = 10^4$ K, and we use the composite calibration from [Murphy et al. \(2011\)](#) which accounts for both thermal and non-thermal contributions to the SFR:

$$\left(\frac{\text{SFR}_\nu}{M_\odot \text{ yr}^{-1}} \right) = 10^{-27} \left[2.18 \left(\frac{T_e}{10^4 \text{ K}} \right)^{0.45} \left(\frac{\nu}{\text{GHz}} \right)^{-0.1} + 15.1 \left(\frac{\nu}{\text{GHz}} \right)^{-\alpha_{\text{NT}}} \right]^{-1} \left(\frac{L_\nu}{\text{erg s}^{-1} \text{ Hz}^{-1}} \right) \quad (6)$$

At 93 GHz, the radio continuum emission from star-forming regions may overlap with the lower-frequency tail of the dust SED. [Wilson et al. \(2019\)](#) estimate a $\sim 10\%$ contribution from dust at 93 GHz for IRAS

13120-5453, NGC 3256, and NGC 7469, the three most IR-luminous galaxies in our sample. We adopt this correction factor of $\sim 10\%$ for all sources, but we acknowledge that the emissivity of dust at 93 GHz may vary between our sources. We further mask pixels that may be contaminated with AGN emission (cf. Table 1).

Variations in T_e and α_{NT} will impact our SFR estimates from the radio continuum at 93 GHz. Electron temperatures typical of HII regions are $T_e \sim 5 \times 10^3 - 10^4$ K, which will produce a change of $\sim 30\%$ ([Murphy et al. 2011](#)). In contrast to this, α_{NT} has been observed as low as ~ 0.5 , which would also give a change in luminosity $\sim 30\%$ at 93 GHz. [Wilson et al. \(2019\)](#) also find evidence of a significant fraction (up to 50%) of non-thermal emission in NGC 7469 at 93 GHz by comparing with an archival radio continuum map at 8 GHz. We adopt an uncertainty of 30% for SFR estimates derived from the radio continuum.

We compare the results of our sample with those of the EMPIRE survey ([Jiménez-Donaire et al. 2019](#)), for which there are publicly-available single-dish (IRAM 30m) observations of HCN and CO. We estimate Σ_{SFR} in EMPIRE galaxies using 24 μm IR maps from the *Spitzer* Space Telescope. These IR data are convolved to a 15'' Gaussian beam utilizing [Aniano et al. \(2011\)](#) Gaussian kernels and further smoothed to a 33'' Gaussian beam using CASA ([McMullin et al. 2007](#)). Backgrounds are subtracted and SFRs are derived using the [Rieke et al. \(2009\)](#) calibration.

2.3.1. Star Formation Timescales and Efficiency

We use the star formation rate (SFR) and molecular gas surface densities to estimate the depletion time of the total (mol = CO) and dense (mol = HCN) molecular

gas content:

$$t_{\text{dep}} = \frac{\Sigma_{\text{mol}}}{\Sigma_{\text{SFR}}} \quad (7)$$

where Σ_{mol} is estimated using Eq. 4. To estimate the dimensionless star formation efficiency, we compare this depletion timescale with the free-fall timescale:

$$t_{\text{ff}} = \sqrt{\frac{3\pi}{32G\rho}} \quad (8)$$

where ρ is a characteristic density of the gas associated with star formation. We calculate gas density assuming a fixed line of sight (LOS) depth via $\rho \approx \Sigma_{\text{mol}}/R$, where R is equivalent to half of the ‘cloud’ or gas depth along the line of sight (LOS). We do not know R , so we assume a fixed value of 100 pc for all galaxies when estimating ρ . We also explored estimating free fall time using the Krumholz et al. (2012) prescriptions for t_{ff} in the GMC and Toomre regimes. We find little qualitative difference in the results between using t_{ff} as described above and the Krumholz et al. (2012) prescription.

The efficiency of the star-formation process is then estimated by comparing the observed depletion timescales with estimates of the free-fall time:

$$\epsilon_{\text{ff}} = \frac{t_{\text{ff}}}{t_{\text{dep}}} \quad (9)$$

which is just the star formation law (Eq. 2) re-written in terms of depletion time.

2.4. Velocity Dispersion

We measure the 1-dimensional velocity dispersion of the molecular gas in our sources, σ_v , using the CO $J = 1 - 0$ transition. The velocity dispersions, $\sigma_{v,\text{meas}}$, are measured directly from moment 2 maps. We correct for broadening of the line due to the finite spectral resolution of our data using Rosolowsky & Leroy (2006):

$$\sigma_v = \sqrt{\sigma_{v,\text{meas}}^2 - \frac{\delta v^2}{2\pi}} \quad (10)$$

where δv is the channel resolution at which we image the data. This value is then converted to the 3-dimensional velocity dispersion via $\sigma_{v,3D} = \sqrt{3}\sigma_v$.

2.4.1. Velocity Dispersion as a Tracer of Mach Number

As previous studies have done for Milky Way clouds (Kainulainen & Federrath 2017), we use CO linewidths as an indicator of the mach number of the gas in our galaxies:

$$\mathcal{M} = \frac{\sqrt{3}\sigma_{v,1D}}{c_s}, \quad (11)$$

where c_s is the thermal sound speed and $\sigma_{v,1D}$ is the observed one-dimensional velocity dispersion. There are limits to this approach, and the ability of the CO line to trace cloud turbulence may be limited by its optical depth (Burkhart et al. 2013; Goodman et al. 2009), and observed line width can include disk rotation or other large-scale motions, but alternative measures of gas kinematics in extragalactic clouds are absent.

To estimate c_s , we consider an ideal gas equation of state ($P_{\text{th}} = nk_{\text{B}}T/\mu m_{\text{H}}$), such that the sound speed is $c_s = \sqrt{k_{\text{B}}T/\mu m_{\text{H}}}$, where k_{B} , T , μ , and m_{H} are the Boltzmann constant, gas kinetic temperature, the mass of a hydrogen atom, and the mean particle weight. For a gas where hydrogen is primarily in molecular form $\mu = 2.33$ (assuming cosmic abundances, Kauffmann et al. 2008). For $\mu = 2.33$ and a temperature range of $T = 10 - 100$ K, $c_s \approx 0.2 - 0.6$ km s⁻¹. The choice of c_s can have a significant impact on the estimate of \mathcal{M} . We choose an intermediate value $c_s = 0.4$ km s⁻¹, corresponding to $T \sim 45$ K as our fiducial value.

2.5. Uncertainties From a Multi-scale Sample

The spatial resolution of the data in our sample span $\sim 50 - 900$ pc. We consider how this range may impact our measurements from the context of a turbulent ISM, and how we can best interpret measured σ_v and line ratios in our sources. The beam filling fraction, $\phi_{\text{ff,beam}}$ is less of an uncertainty in this study, since the sources with the lowest resolution are (U)LIRGs and likely have filling fractions approaching unity, while the spiral galaxy centers have resolutions approaching cloud scales. This reduces the issue of variations in beam filling fractions from galaxy-to-galaxy. A significant source of uncertainty instead comes from variations in the relative filling fractions of the HCN/CO transitions:

$$\Phi_{\text{HCN/CO}} \approx \frac{r_{\text{HCN}}^2}{r_{\text{CO}}^2}, \quad (12)$$

where r_{HCN} and r_{CO} are the average radial extents of HCN and CO, respectively. We explore variations in the filling fraction in Bemis (2020) and Bemis & Wilson, in prep. from a radiative transfer perspective.

In addition to the uncertainty in $\Phi_{\text{HCN/CO}}$, the velocity dispersion in a turbulent medium is scale-dependent (ℓ) such that (Larson 1981; Heyer et al. 2009):

$$\sigma_v(\ell) = \sigma_{v,L} \left(\frac{\ell}{L}\right)^p \quad (13)$$

where $p \sim 0.33 - 0.5$ depends on the type of turbulence, (e.g. $p \approx 0.33$ for Kolmogorov, Larson 1981), L can be defined as the cloud diameter (or turbulent injection scale) and $\sigma_{v,L}$ is the cloud dispersion at that

scale. A sample of galaxies at different physical scales will therefore be affected by this scale dependence, such that velocity dispersions will be smaller at smaller scales and vice versa. However, this relationship should saturate at the turbulent injection scale, which may mitigate some of this uncertainty. If larger-scale cloud-cloud motions do not affect the velocity dispersions of CO, then this saturation should be detected, although there is still uncertainty in L . This means that lower-resolution observations may still be useful for assessing σ_v .

3. MODEL FRAMEWORK: GRAVOTURBULENT MODELS OF STAR FORMATION

We consider several prescriptions of f_{grav} in the context of analytical models of star formation, and compare the predictions of these models to measurements of the $I_{\text{HCN}}/I_{\text{CO}}$ ratio and the star formation properties of our galaxies. We use Eq. 2, which is relevant to gravoturbulent models of star formation (KMD12).

ϵ_{ff} is calculated by integrating over the star-forming portion of the density-weighted gas density Probability Distribution Function (PDF, e.g. Krumholz & McKee 2005; Padoan & Nordlund 2011; Hennebelle & Chabrier 2011; Federrath & Klessen 2012):

$$\epsilon_{\text{ff}} = \epsilon_0 \int_{n_{\text{SF}}}^{\infty} \frac{t_{\text{ff}}(n_0)}{t_{\text{ff}}(n)} \frac{n}{n_0} p(n) dn \quad (14)$$

Here $p(n)$ is the cloud's volumetric density PDF, n -PDF, and n_0 is its mean density. The n -PDF characterizes the distribution of densities of *all* gas within the cloud, including the diffuse atomic and molecular components. We briefly review specific terms within this equation individually.

$p(n)$: Isothermal gas in the presence of supersonic turbulence naturally becomes distributed such that its n -PDF is roughly lognormal (Vazquez-Semadeni 1994; Nordlund & Padoan 1999; Wada & Norman 2001). Earlier formalisms of gravoturbulent models adopt a purely lognormal form of $p(n)$ (e.g. Krumholz & McKee 2005; Padoan & Nordlund 2011; Federrath & Klessen 2012). In terms of the logarithmic volume density $s = \ln(n/n_0)$, this is given by:

$$p_s = N \frac{1}{\sqrt{2\pi\sigma_s^2}} \exp\left(-\frac{(s-s_0)^2}{2\sigma_s^2}\right) \quad (15)$$

where N is a normalization constant⁷, σ_s^2 is the logarithmic density variance which depends on the underlying physics of the gas and sets the width of $p(n)$, and $s_0 = -0.5\sigma_s^2$. Newer formalisms (i.e. Burkhart 2018)

of gravoturbulent models of star formation suggest that the n -PDF may then evolve to include a high-density powerlaw tail which contains gas that is becoming gravitationally unstable to collapse. Observations of clouds in the Milky Way support a composite form of $p(n)$, where a powerlaw tail is clearly present in addition to a more-diffuse component of gas. Burkhart (2018) presents this as a piecewise function:

$$p_s = \begin{cases} N \frac{1}{\sqrt{2\pi\sigma_s^2}} \exp\left(-\frac{(s-s_0)^2}{2\sigma_s^2}\right), & s < s_t \\ NCe^{-\alpha_{\text{PL}}s}, & s > s_t \end{cases} \quad (16)$$

where s_t is the logarithmic form of the transition density between the two components of the n -PDF, and α_{PL} is the slope of the powerlaw tail. The factors N and C are normalization constants given by Burkhart (2018).

σ_s : Numerical studies have shown that if the turbulence is super-Alfvénic, and the magnetic field (B) follows a powerlaw relationship with gas density, $B \propto n^{1/2}$, then the logarithmic density variance is given by (Molina et al. 2012; Federrath & Klessen 2012):

$$\sigma_s^2 = \ln\left(1 + b^2 \mathcal{M}^2 \frac{\beta}{\beta + 1}\right) \quad (17)$$

where \mathcal{M} is the mach number, $\beta = P_{\text{th}}/P_{\text{mag}}$ is the plasma beta (which characterizes the ratio of thermal pressure to magnetic pressure), and b is the turbulent forcing parameter (which characterizes the relative amount of solenoidal $b = 1$ or compressive $b = 0.33$ turbulence within the gas). Without a clear prescription for β and b in our sample, we simply take $\beta \rightarrow \infty$, which assumes that $B = 0$ G. We take an intermediate value $b = 0.4$, which assumes that turbulence is a mixture of compressive and solenoidal forcing. Non-isothermal gas will add intermittency resulting in deviations from a lognormal shape of $p(n)$ (Federrath & Banerjee 2015). For the purpose of this work, we assume an underlying lognormal is a reasonable, intermediate approximation to part of the n -PDF (Federrath & Banerjee 2015).

n_{SF} : Gravity overcomes supportive processes and begins the process of collapse above the density threshold, n_{SF} . The processes competing with gravity include some combination of magnetic support, internal turbulent motions, external ISM pressures, etc. Any gas with densities higher than n_{SF} is then potentially gravitationally unstable and star-forming, so n_{SF} serves as the lower limit of the integration that determines ϵ_{ff} .

$t_{\text{ff}}(n_0)/t_{\text{ff}}(n)$: Within the integral in Eq. 14 integral is a free-fall time factor, which converts the integrand into a dimensionless mass *rate* equivalent to the mass per free-fall time (Federrath & Klessen 2012). This time factor is treated differently depending on the analytical

⁷ We use N given by Burkhart (2018).

model being considered, e.g. single free-fall (SFF) time (Krumholz & McKee 2005; Padoan & Nordlund 2011) versus multi-free-fall (MFF) time models (Hennebelle & Chabrier 2011; Federrath & Klessen 2012), and these differences are summarized in Federrath & Klessen (2012) and Burkhardt (2018). MFF models keep this factor in the integral, which predicts different rates of collapse for different densities, while SFF models take this factor out of the integral. Due to this difference, MFF models predict higher ϵ_{ff} .

ϵ_0 : The prefactor in Eq. 14, ϵ_0 , is the *local* dimensionless efficiency of star formation. ϵ_0 depends on additional processes, such as the level of stellar feedback dispelling some of the gas that is already above n_{SF} (Burkhardt & Mocz 2019). The mass that does get converted into stars is then $M_* = \epsilon_0 M(n > n_{\text{SF}})$.

3.1. Different Formalisms of Gravoturbulent Models of Star Formation

Federrath & Klessen (2012) and Burkhardt (2018) both provide analytical equations for estimating ϵ_{ff} for different gravoturbulent formalisms which we adopt in this analysis. In this work, we focus on three analytical models which each have unique prescriptions for the density threshold and the shape of the n -PDF: 1. the Padoan & Nordlund (2011) formalism, 2. the Burkhardt (2018) and Burkhardt & Mocz (2019) formalism, and 3. a fixed density threshold model, which is not explicitly formulated in previous works but is often referenced in the literature when interpreting the results of studies using dense gas tracers (e.g. Gao & Solomon 2004a,b).

We mainly refer to analytical equations from Burkhardt (2018) for brevity, but also refer the reader to Federrath & Klessen (2012) for another comprehensive summary of analytical models, as well as the original papers that have provided the basis of this work, e.g. Krumholz & McKee (2005); Padoan & Nordlund (2011); Hennebelle & Chabrier (2011). We summarize the following important quantities of each of the models we use in this work: (a) the underlying n -PDF shape of the model, $p(n)$; (b) the equation used to estimate ϵ_{ff} ; (c) the star formation threshold density, n_{SF} ; (d) and the method we use to determine f_{grav} :

1. The Padoan & Nordlund (2011) formalism:

- (a) These models have a lognormal (LN) n -PDF (see Eq. 15).

- (b) Padoan & Nordlund (2011) estimate ϵ_{ff} using (cf. Eq. (13) in Burkhardt 2018):

$$\epsilon_{\text{ff,PN11}} = \frac{\epsilon_0}{2} \left\{ 1 + \operatorname{erf} \left(\frac{\sigma_2^2 - 2 s_{\text{thresh}}}{\sqrt{8} \sigma_s} \right) \right\} \times \exp(s_{\text{thresh}}/2) \quad (18)$$

where $s_{\text{thresh}} = \exp(n_{\text{SF}}/n_0)$.⁸

- (c) The Padoan & Nordlund (2011) equation for n_{SF} that determines s_{thresh} in Eq. 18 is given by (cf. Eq. (11) in Burkhardt (2018)):

$$n_{\text{SF}} \approx 0.54 n_0 \alpha_{\text{vir}} \mathcal{M}^2 \quad (19)$$

when we have taken the prefactor in their original equation to be $\phi = 0.35$ and have neglected magnetic fields. The remaining dependence is then only with mean density, virial parameter (α_{vir}), and \mathcal{M} .⁹ We can also rewrite this equation in terms of the turbulent pressure, which we are able to estimate directly from our data (cf. Walker et al. 2018):

$$n_{\text{SF}} \approx 0.36 \alpha_{\text{vir}} \frac{P_{\text{turb}}}{k_B T_{\text{kin}}} \quad (20)$$

where $P_{\text{turb}} \approx (3/2)\Sigma_{\text{mol}}\sigma_v^2/R$ or $P_{\text{turb}} \approx (3/2)n_0\sigma_v^2$ for the data and models, respectively. The direct scalings $n_{\text{SF}} \propto \mathcal{M}^2$ and $n_{\text{SF}} \propto P_{\text{turb}}$ assume that turbulence acts as a supportive process to the gas. The virial parameter, α_{vir} , is given by:

$$\alpha_{\text{vir}} \approx \frac{5\sigma_v^2 R}{G\Sigma} \quad (21)$$

and is the ratio of internal kinetic to gravitational energy in a cloud, E_{kin} and E_{grav} .

- (d) For these models, we perform a numerical integration of the n -PDF above n_{SF} (Eq. 19) to calculate f_{grav} .¹⁰

2. The Burkhardt (2018) and Burkhardt & Mocz (2019) formalism:

⁸ This formula is almost identical to the Krumholz & McKee (2005) formalism for ϵ_{ff} if we remove the exponential factor containing s_{thresh} .

⁹ This equation is nearly identical to the Krumholz & McKee (2005) formalism, which has a prefactor $\pi/15$ (assuming $\phi_t = 1$).

¹⁰ n_{SF} is referred to as n_{crit} in Padoan & Nordlund (2011) and Burkhardt (2018), not to be confused with the critical density for a molecular transition.

- (a) These models have a piecewise (lognormal plus powerlaw, LN+PL) n -PDF (cf. Eq. 16).
- (b) (Burkhart 2018) calculate ϵ_{ff} using a composite LN+PL n -PDF (cf. Eq. (27) in Burkhart 2018):

$$\epsilon_{\text{ff,BM18}} = N \exp(s_{\text{thresh}}/2) \frac{\epsilon_0}{2} \left\{ \text{erf} \left(\frac{\sigma_2^2 - 2 s_{\text{thresh}}}{\sqrt{8}\sigma_s} \right) - \text{erf} \left(\frac{\sigma_2^2 - 2 s_t}{\sqrt{8}\sigma_s} \right) + C \frac{\exp(s_t(1 - \alpha_{\text{PL}}))}{\alpha_{\text{PL}} - 1} \right\} \quad (22)$$

where s_t is the density at which the n -PDF transitions from a lognormal to power law shape, and N is a normalization factor. We take $s_{\text{thresh}} \equiv s_t$.

- (c) We adopt s_t as the threshold density for the Burkhart (2018) formalism, which is given in Burkhart & Mocz (2019) as:

$$s_t = (\alpha_{\text{PL}} - 1/2)\sigma_s^2. \quad (23)$$

In this formalism, s_t is tied to the slope of the PL component of the n -PDF, as well as the width of the lognormal component.

- (d) For the LN+PL models, f_{grav} is given by Eq. (20) in Burkhart & Mocz (2019) (which is referred to as f_{dense} in their work).

3. Fixed density threshold models:

- (a) These models have a lognormal (LN) n -PDF (see Eq. 15).
- (b) We again use Eq. (13) from Burkhart (2018) to calculate ϵ_{ff} .
- (c) We use a fixed density threshold of $n_{\text{SF}} = 10^{4.5} \text{ cm}^{-3}$.
- (d) We perform a numerical integration of the n -PDF above n_{SF} to calculate f_{grav} .

We hereafter refer to these three models as (1) LN PN11, (2) LN+PL B18, and (3) LN Fixed.

3.2. Predictions of Analytical Models

Each of the models above has a unique prescription for f_{grav} depending on n_{SF} and the shape of the n -PDF, and this has an impact on their predictions of star formation. The simplest prescription for f_{grav} is that of fixed density-threshold models, which predict that

$n_{\text{SF}} \approx 10^{4.5} \text{ cm}^{-3}$. In this context, the fraction of star-forming gas is any gas above this density. For purely lognormal n -PDFs, increases in the width of the n -PDF, σ_n , and mean density will both contribute to higher f_{grav} and subsequently higher ϵ_{ff} . This model implies that the SFR is set solely by mass available above $n_{\text{SF}} \approx 10^{4.5} \text{ cm}^{-3}$, and that the depletion time of this dense gas mass is constant.

A fixed density threshold also has several other testable predictions:

- Higher \mathcal{M} increases σ_v and so contributes to *higher* f_{grav} , shorter total gas depletion times, and ultimately higher Σ_{SFR} . As a result, for a given \mathcal{M} , only the increase in gas mass (Σ_{mol}) is important for increasing Σ_{SFR} .
- Higher mean densities correlate with *higher* f_{grav} , shorter total gas depletion times, and ultimately higher Σ_{SFR} .

The Burkhart (2018) and Padoan & Nordlund (2011) models predict that n_{SF} varies, but these formalisms have different interpretations as to why this variation occurs. Burkhart (2018) argue that variations in ϵ_{ff} may largely be linked to evolutionary changes in the n -PDF shape such that the n -PDF evolves from a lognormal shape to a composite lognormal and powerlaw over time, and the PL tail develops a shallower slope as more gas becomes gravitationally-bound (cf. Ballesteros-Paredes et al. 2011).

There is a dependence also on turbulence similar to that of the Padoan & Nordlund (2011) model, but Burkhart (2018) argue that this dependence becomes less important as clouds become more evolved (i.e. α_{PL} becomes more shallow). The Burkhart (2018) model also does not depend on explicitly on α_{vir} , whereas virialization of the gas is included in the Padoan & Nordlund (2011) definition of n_{SF} .

In the Burkhart (2018) and Padoan & Nordlund (2011) models, higher \mathcal{M} has the effect of increasing n_{SF} . Based on this, the following qualitative predictions can then be made about both of these models:

- Clouds with higher \mathcal{M} (higher P_{turb}) can have a broader n -PDF and higher n_{SF} , *lower* f_{grav} , *lower* star formation efficiencies, and ultimately smaller Σ_{SFR} .
- Higher temperatures reduce \mathcal{M} , and may *decrease* n_{SF} and potentially *increase* f_{grav} and *enhance* star formation efficiencies. This effect will likely be much smaller than changes in P_{turb} , which can span > 5 orders of magnitude, compared to T_{kin} which only can span ~ 2 orders of magnitude.

We note that the major difference between the predictions for a fixed n_{SF} and one that varies as $n_{\text{SF}} \propto \mathcal{M}^2$ is whether \mathcal{M} directly enhances or suppresses star formation. For the LN+PL B18 models, smaller values of α_{PL} (i.e. shallower slopes) will result in more mass in the PL tail and higher f_{grav} , which will ultimately *enhance* ϵ_{ff} . We consider these differences when we are comparing the predictions of these analytical models with our data in the §4.

3.3. Connecting Observations to Theory

To compare models with data from our sample, we create a sets of models for each of the three, unique prescriptions. We produce LN models over the $\sigma_v^2/R - \Sigma_{\text{mol}}$ parameter space that encompasses our data in Fig. 1. For comparison, we also show the Sun et al. (2018) measurements of cloud-scale observations in nearby galaxies in Fig. 1. The mean trend of this parameter space is the empirical trend between velocity dispersion and molecular gas surface density found by Sun et al. (2018) for a subset of PHANGS galaxies at cloud-scales:

$$\log_{10} \left(\frac{\sigma_v}{\text{km s}^{-1}} \right) = \log_{10} \left(\frac{\Sigma_{\text{mol}}}{10^2 M_{\odot} \text{ pc}^{-2}} \right) + 0.85 \quad (24)$$

This is shown in Fig. 1 as the dotted line. Sun et al. (2018) assume a radius of 40 pc for their sources. Since we assume a fixed LOS depth of 100 pc, we scale the right side of Eq. 24 by a factor of $\sqrt{100 \text{ pc}/40 \text{ pc}}$.

The vertical spread in Fig. 1 is from variations in σ_v that we consider for the LN models, and roughly reproduces the spread in $\sigma_v^2/R - \Sigma_{\text{mol}}$ seen in the Sun et al. (2018) sample as well as our sample of galaxies. For the LN+PL B18 models, we impose Eq. 24 and consider a range of $\alpha_{\text{PL}} = 1.0 - 2.3$, instead of the range in σ_v considered for the LN models.

We note that the observational efficiency is estimated by taking the ratio of the free-fall time to the depletion time, $\epsilon_{\text{ff}} = t_{\text{ff}}/t_{\text{dep}}$. As Burkhart & Mocz (2019) point out, a more physically-meaningful efficiency for observations of individual star forming clouds may be the local *instantaneous* efficiency of star formation at time t , $\epsilon_{\text{inst}} \approx \epsilon_0(t) f_{\text{grav}}(t)$, where $\epsilon_{\text{inst}} < \epsilon_{\text{ff}}$. This in particular applies to clouds that have evolved sufficiently to have a powerlaw tail, where f_{grav} is the fraction of mass that is gravitationally-bound (and therefore in the powerlaw tail). ϵ_{ff} itself is an *average* of the star formation efficiency of a cloud over the free-fall time, which is not directly observable. For simplicity we assume our observational estimates of ϵ_{ff} are indeed sensitive to the theoretical definition of ϵ_{ff} . We also compare observational trends of ϵ_{ff} with model trends of $f_{\text{grav}} \propto \epsilon_{\text{inst}}$.

We adopt a constant, local efficiency of $\epsilon_0 = 1\%$ for all models. This value of ϵ_0 is consistent with estimates of

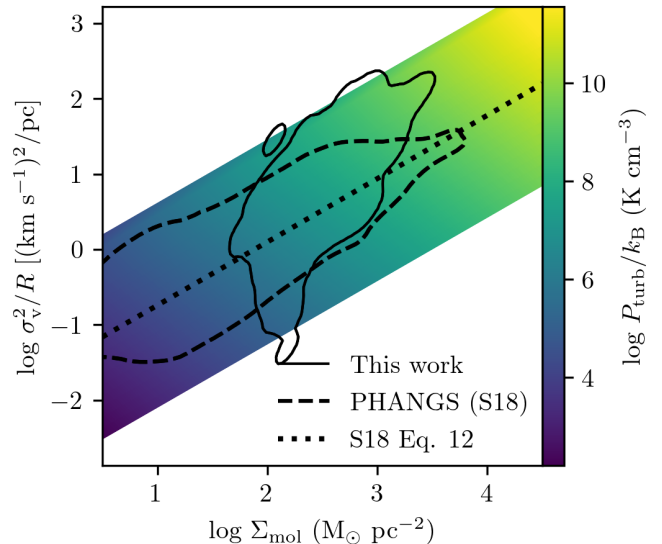


Figure 1. The grid of cloud coefficients, σ_v/R^2 , (cf. Heyer et al. 2009) and molecular gas surface densities, Σ_{mol} , used as inputs to the lognormal-only analytical models, colored by turbulent pressure, P_{turb} . The x -axis is proportional to model mean density. The data are shown as the contour density plots, with our sample contained within the solid black line, and the locus of the Sun et al. (2018) cloud-scale measurements as the dashed black contour. We use Eq. 12 from Sun et al. (2018) to define the mean relationship between Σ_{mol} and σ_v in our model parameter space (dotted black line).

ϵ_{ff} from observations, and simulations imply low efficiencies, which range from 0.01– $\lesssim 20\%$ (Evans et al. 2009; Lada et al. 2010; Ostriker & Shetty 2011; Krumholz 2014; Zamora-Avilés & Vázquez-Semadeni 2014; Lee et al. 2016; Semenov et al. 2017; Grudić et al. 2018). We summarize the observational measurements and the quantities that we estimate from them in the top half of Table 2. In the bottom half of Table 2 we list the equations used to estimate the same quantities using model outputs.

4. RESULTS

In this section we review general trends between observation-based quantities and the predictions of those from analytical models of star formation. We present a series of plots showing the observational quantities listed in the top half of Table 2 that we will use to compare against the model predictions described in the bottom half of Table 2. We focus on variations in star formation timescales (depletion time and free-fall time), star formation efficiency, and the dense gas fraction. We do not directly assess variations in emissivity in this paper, and defer an analysis of emissivity (and therefore conversion factors) to Bemis (2020) and Bemis

Table 2. Observational quantities (top panel) compared to model inputs and outputs (bottom panel).

	Observational Estimate	Eqn.	Unit
	$\Sigma_{\text{mol,obs}}$	$\alpha_{\text{CO}} (I_{\text{CO}} / \text{K km s}^{-1})$	$M_{\odot} \text{ pc}^{-2}$
	$\Sigma_{\text{mol,dense,obs}}$	$3.2 \alpha_{\text{CO}} (I_{\text{HCN}} / \text{K km s}^{-1})$	$M_{\odot} \text{ pc}^{-2}$
(1)	$\Sigma_{\text{SFR,obs}}$	$1.14 \times 10^{-29} (L_{93 \text{ GHz}} / \text{erg s}^{-1} \text{ Hz})$	$M_{\odot} \text{ yr}^{-1} \text{ kpc}^{-2}$
(2)	$P_{\text{turb,obs}}$	$(3/2) \Sigma_{\text{mol}} \sigma_v^2 / R / k_{\text{B}}$	K cm^{-3}
(3)	$t_{\text{dep,obs}}$	$\Sigma_{\text{mol}} / \Sigma_{\text{SFR}}$	yr
	$n_{0,\text{obs}}$	Σ_{mol} / R	kg cm^{-3}
	$t_{\text{ff,obs}}$	$\sqrt{3\pi/32 G n_{0,\text{obs}}}$	yr
(4)	$\epsilon_{\text{ff,obs}}$	$t_{\text{ff,obs}} / t_{\text{dep,obs}}$	–
(5)	f_{dense}	$3.2 I_{\text{HCN}} / I_{\text{CO}}$	–
(6)	$t_{\text{dep,dense,obs}}$	$\Sigma_{\text{mol,dense}} / \Sigma_{\text{SFR}}$	yr
	Model Estimates	Eqn.	Unit
(1)	$\Sigma_{\text{SFR,model}}$	$\epsilon_{\text{ff,model}} \times \Sigma_{\text{mol,grid}} / t_{\text{ff,grid}}$	$M_{\odot} \text{ yr}^{-1} \text{ kpc}^{-2}$
(2)	$P_{\text{turb,model}}$	$(3/2) n_0 \sigma_v^2 / k_{\text{B}}$	K cm^{-3}
(3)	$t_{\text{dep,model}}$	$1 / \epsilon_{\text{ff,model}} \times t_{\text{ff,grid}}$	yr
(4)	$\epsilon_{\text{ff,model}}$	Eq. (13) or (27) in Burkhart (2018)	–
(5)	f_{grav}	Eq. 1, Eq. (20) in Burkhart & Mocz (2019)	–
(6)	$t_{\text{dep,grav}}$	$f_{\text{grav}} / \epsilon_{\text{ff,model}} \times t_{\text{ff,grid}}$	yr
(6)	$t_{\text{dep,dense,model}}$	$f(n > 10^{4.5} \text{ cm}^{-3}) / \epsilon_{\text{ff,model}} \times t_{\text{ff,grid}}$	yr

NOTES – We number matching observational and model analogs in the leftmost column. We fix $T_{\text{kin}} = 45 \text{ K}$, $b = 0.4$, and $\beta \rightarrow \infty$ in this analysis, and we model over the observed ranges of Σ_{mol} and σ_v . Quantities with the subscript ‘grid’ are input from the grid shown in Fig. 1.

& Wilson, in prep., where we present modelling of the HCN and CO emissivities for our sample of galaxies on a pixel-by-pixel basis.

The results from analytical models are compared to the data in Figures 2-11. We consider fiducial models which correspond to the parameters that best fit the observed Kennicutt-Schmidt relationship (see Fig. 3). For each model, we calculate the χ^2 of the data relative to this fiducial model, and this value is shown in each panel. We note that the best fit value for α_{PL} is 1.9 for the LN+PL models. The best fit-relationship between $\Sigma_{\text{mol}} - \sigma_v$ for the LN-only models is in agreement with the [Sun et al. \(2018\)](#) relationship (Eq. 24), within uncertainty.

We show separate plots with only the data and their measurement uncertainties, followed by plots comparing the data with the models. We refer to Spearman rank coefficients as a measure of the strength and direction of correlations between two parameters. For reference, a coefficient of $r_s = 0$ indicates that there is no monotonic relationship between the two parameters, negative values indicate negative monotonic relationships, and positive values indicate positive monotonic relationships. In the following discussion, we use the following definitions: $0.1 \leq |r_s| < 0.4$ is considered a weak correlation,

$0.4 \leq |r_s| < 0.7$ is considered a moderate correlation, and $|r_s| \geq 0.7$ is considered a strong correlation.

4.1. The Kennicutt-Schmidt Relationship

We begin by presenting the Kennicutt-Schmidt (KS) relationship of our data in Fig. 2. In Fig. 3 we compare the data to model predictions of Σ_{SFR} , which are determined using the relevant equation in Table 2 and the parameter spaces discussed in §3.3.

1. *LN PN11*: The LN models with the varying [Padoan & Nordlund \(2011\)](#) threshold produce a steeper relationship than observed at lower gas surface densities. The (U)LIRGs studied in [Wilson et al. \(2019\)](#) show a double power-law Kennicutt-Schmidt relationship, with lower Σ_{mol} galaxies returning a slope close to unity, similar to the results of [Bigiel et al. \(2008\)](#). The higher- Σ_{mol} galaxies instead have a steeper Kennicutt-Schmidt slope of 1.74. For the parameter space we consider, the trend of the Kennicutt-Schmidt relationship predicted by the PN11 models is in agreement with a slope > 1 .
2. *LN+PL B18*: Similar to the PN11 models, the LN+PL B18 models produce a steeper relationship than observed at lower gas surface densities, and

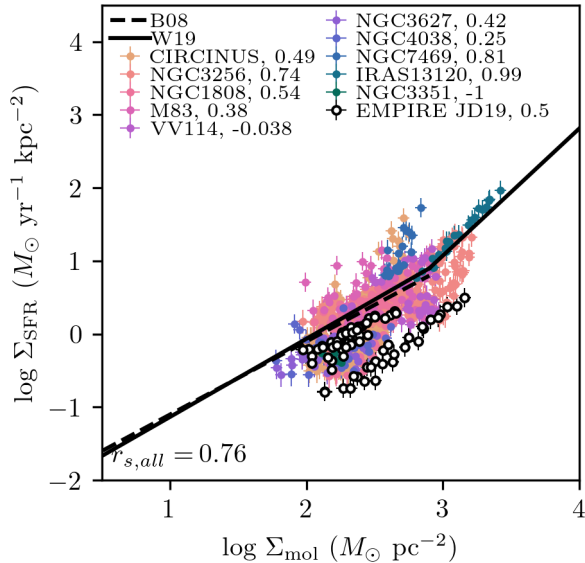


Figure 2. The Kennicutt-Schmidt relationship for our galaxies and the EMPIRE sample. Data is shown for our sample (colored by galaxy) and the EMPIRE galaxies (white points). We also include fits to this relationship from previous studies (e.g. nearby disk galaxies from Bigiel et al. 2008, B08, and (U)LIRGs from Wilson et al. (2019), W19). Spearman rank coefficients are shown for individual galaxies next to their name in the legend, and the coefficient for the combined sample is shown in the lower left corner. On average, the galaxies in the EMPIRE sample have lower Σ_{SFR} than the galaxies in our sample, despite similar gas surface densities. Compared to the normal disk galaxies of the EMPIRE sample, the galaxies in our sample are more extreme and include mergers, U/LIRGs, and galaxy centers (cf. Table 1.)

match the steep slope observed by Wilson et al. (2019) for U/LIRGs. We find larger α_{PL} results in lower Σ_{SFR} (left panel of Fig. 3), in agreement with the predictions from Burkhardt (2018). Burkhardt (2018) argue that larger α_{PL} results in lower ϵ_{ff} (and higher Σ_{SFR}), which is seen for some Milky Way clouds.

3. *LN Fixed:* These fixed-threshold models produce a trend in Σ_{SFR} with Σ_{mol} that is not seen in the data. Lower Σ_{mol} values produce a steeper Kennicutt-Schmidt relation, while higher Σ_{mol} produce a shallower Kennicutt-Schmidt relation, in conflict with what is observed.

Figure 3 demonstrates that each model is able to reproduce some of the scatter of the Kennicutt-Schmidt relationship when considering variations in α_{PL} (LN+PL B18 models) and σ_{v} (LN models) for a given gas surface density. No models produce a multi-slope Kennicutt-Schmidt relationship consistent with

the slopes measured in previous studies (e.g. Wilson et al. 2019). However, we note that changing the slope of the imposed relationship between σ_{v} and Σ_{mol} (Fig. 1) has the effect of changing the slope of the Kennicutt-Schmidt relation for all of these models. Lower slopes, e.g. $\log \sigma_{\text{v}} \propto 0.1 \log \Sigma_{\text{mol}}$, produce a shallower Kennicutt-Schmidt relation. We cannot exclude the possibility that other model parameters (i.e. b , β , and T_{kin}) may have underlying trends with Σ_{mol} or σ_{v} , which could in turn also produce a varying Kennicutt-Schmidt slope. Additionally, ϵ_0 could vary with Σ_{mol} , for example if a higher Σ_{SFR} results in higher stellar feedback and a lower ϵ_0 . Variations in PL slope may also contribute to changes in the slope of the Kennicutt-Schmidt relation. Federrath & Klessen (2013) find that decreases in power law slope coincide with enhanced star formation efficiencies and vice versa (Burkhart & Mocz 2019; Federrath & Klessen 2013), and that this is a reflection of the increased fraction of dense gas that coincides with shallow power law slopes. To match the shallower slope of the KS relationship at gas surface densities below $\Sigma_{\text{mol}} \approx 10^{2.9} M_{\odot} \text{pc}^{-2}$ (Bigiel et al. 2008; Wilson et al. 2019; Kennicutt & De Los Reyes 2021, e.g.), the average PL slope would need to increase (become steeper) towards higher gas surface densities. This would also imply lower ϵ_0 towards higher Σ_{mol} (Burkhart & Mocz 2019; Federrath & Klessen 2013). Above $\Sigma_{\text{mol}} \approx 10^{2.9} M_{\odot} \text{pc}^{-2}$, the steeper KS slope found in Wilson et al. (2019) appears consistent with a constant PL slope.

4.2. Does HCN/CO trace the Star-forming Gas Fraction?

We compare the observed dense gas fraction ($f_{\text{dense}} = \alpha_{\text{HCN}}/\alpha_{\text{CO}} I_{\text{HCN}}/I_{\text{CO}}$) with estimates of turbulent pressure, P_{turb} , in Fig. 4. Our data, on average, show a weak positive trend between f_{dense} and P_{turb} , and this relation also holds within most of the individual galaxies in our sample. We plot model predictions of f_{grav} vs. P_{turb} in Fig. 5, and show the outline of the data relationship between f_{dense} and P_{turb} in the background. For comparison, in the bottom rows of Fig. 5 we plot the fraction of gas above a fixed density $n = 10^{4.5} \text{cm}^{-3}$ for all of the three model n -PDFs prescriptions.

1. *LN PN11:* The LN varying threshold models also predict a negative trend between f_{grav} and P_{turb} . On average f_{grav} is lower than f_{dense} predicted by the data. Similar to the LN+PL B18 models, we see a positive trend between $f(n > 10^{4.5} \text{cm}^{-3})$ and P_{turb} . However, there is very little spread in the model $f(n > 10^{4.5} \text{cm}^{-3})$ vs P_{turb} relationship. This indicates that the spread observed in

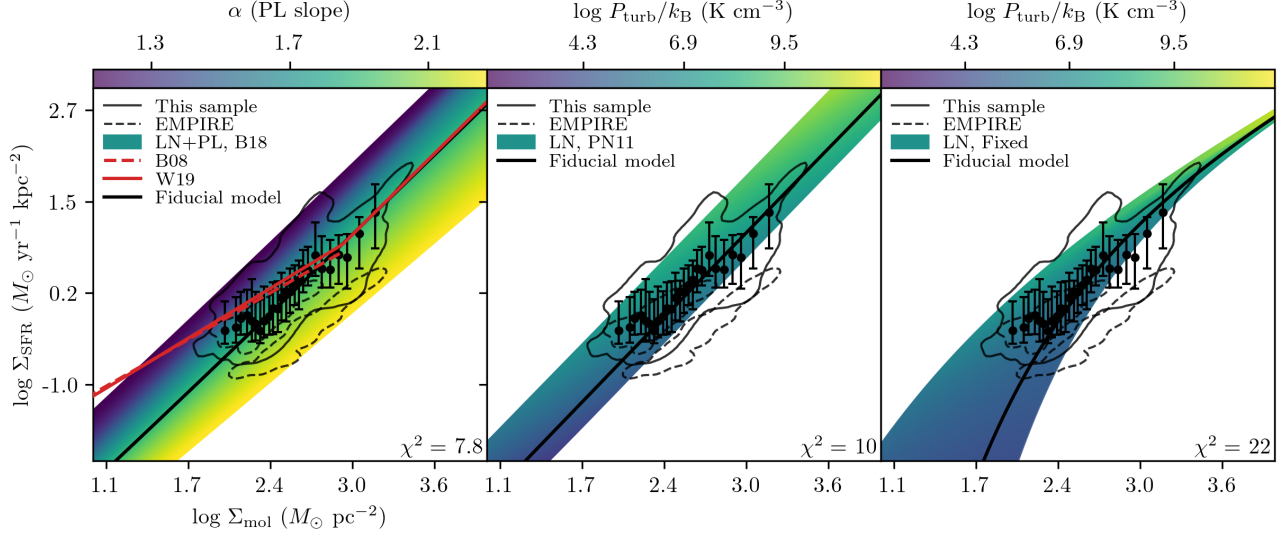


Figure 3. The Kennicutt-Schmidt relationship for our galaxies (solid black contours) and the EMPIRE sample (dashed black contours), compared to the model predictions. We also include fits to this relationship from previous studies (see Fig. 2 caption). The three models we consider in this analysis are: the LN+PL B18 model with varying n_{SF} (left), the LN model with the Padoan & Nordlund (2011) n_{SF} (center), and the LN model with a fixed $n_{\text{SF}} = 10^{4.5} \text{ cm}^{-3}$ (right). The LN+PL B18 models are colored by α_{PL} , and the LN models are colored by P_{turb} . χ^2 relative to the fiducial model is shown in the lower right corner of each plot. The median values of the data are shown with the black datapoints, and the errorbars correspond to the $1 - \sigma$ spread in each bin.

Each model is able to reproduce some of the scatter of the Kennicutt-Schmidt relationship when considering variations in α_{PL} (LN+PL B18 models) and $P_{\text{turb}} \propto \sigma_v^2$ (LN models) for a given gas surface density.

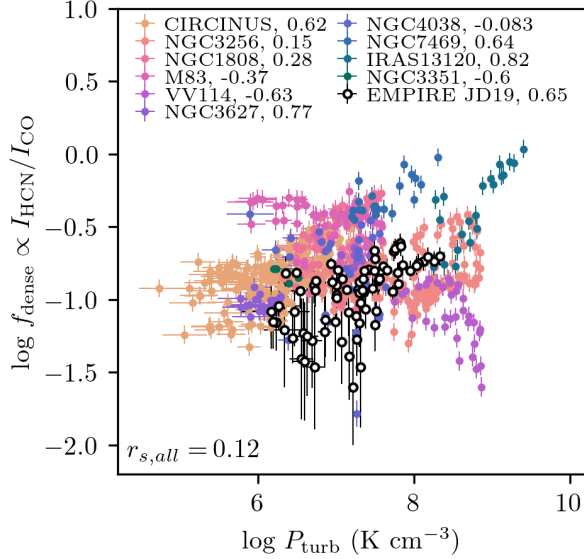


Figure 4. Dense gas fraction as a function of turbulent pressure for our galaxies and the EMPIRE sample, where $f_{\text{dense}} = \alpha_{\text{HCN}}/\alpha_{\text{CO}} I_{\text{HCN}}/I_{\text{CO}}$. Correlation coefficients are shown and data is colored by galaxy, similar to the formatting in Fig. 2. The sample as a whole shows a weak, positive correlation between f_{dense} traced by $I_{\text{HCN}}/I_{\text{CO}}$ and P_{turb} . The disk galaxies in the EMPIRE sample show a strong, positive correlation.

the f_{dense} vs. P_{turb} relationship in our data is not well-reproduced by variations in σ_v alone.

2. *LN+PL B18:* For constant α_{PL} , these models predict a negative trend between f_{grav} and P_{turb} , and this becomes steeper for larger α_{PL} . The data primarily overlap with f_{grav} for models with shallower values of α_{PL} . In contrast, we see a positive trend between $f(n > 10^{4.5} \text{ cm}^{-3})$ predicted by the models and P_{turb} . Lower values of α_{PL} produce a flatter relationship between $f(n > 10^{4.5} \text{ cm}^{-3})$ at low P_{turb} . This results in a broader spread in this relationship at lower P_{turb} . In general, the spread observed in the f_{dense} vs. P_{turb} relationship in our data is not well-reproduced by variations in α_{PL} alone.
3. *LN Fixed:* f_{grav} predicted by the fixed-density threshold models is identical to $f(n > 10^{4.5} \text{ cm}^{-3})$, since we set the threshold for these models to $n = 10^{4.5} \text{ cm}^{-3}$. As with the other models, we see a positive relationship between $f(n > 10^{4.5} \text{ cm}^{-3})$ and P_{turb} . The spread in the data is not well-reproduced by these models.

The predictions of f_{grav} from the varying threshold models show negative trends with P_{turb} for constant α_{PL} (LN+PL B18 models), in contrast to the positive

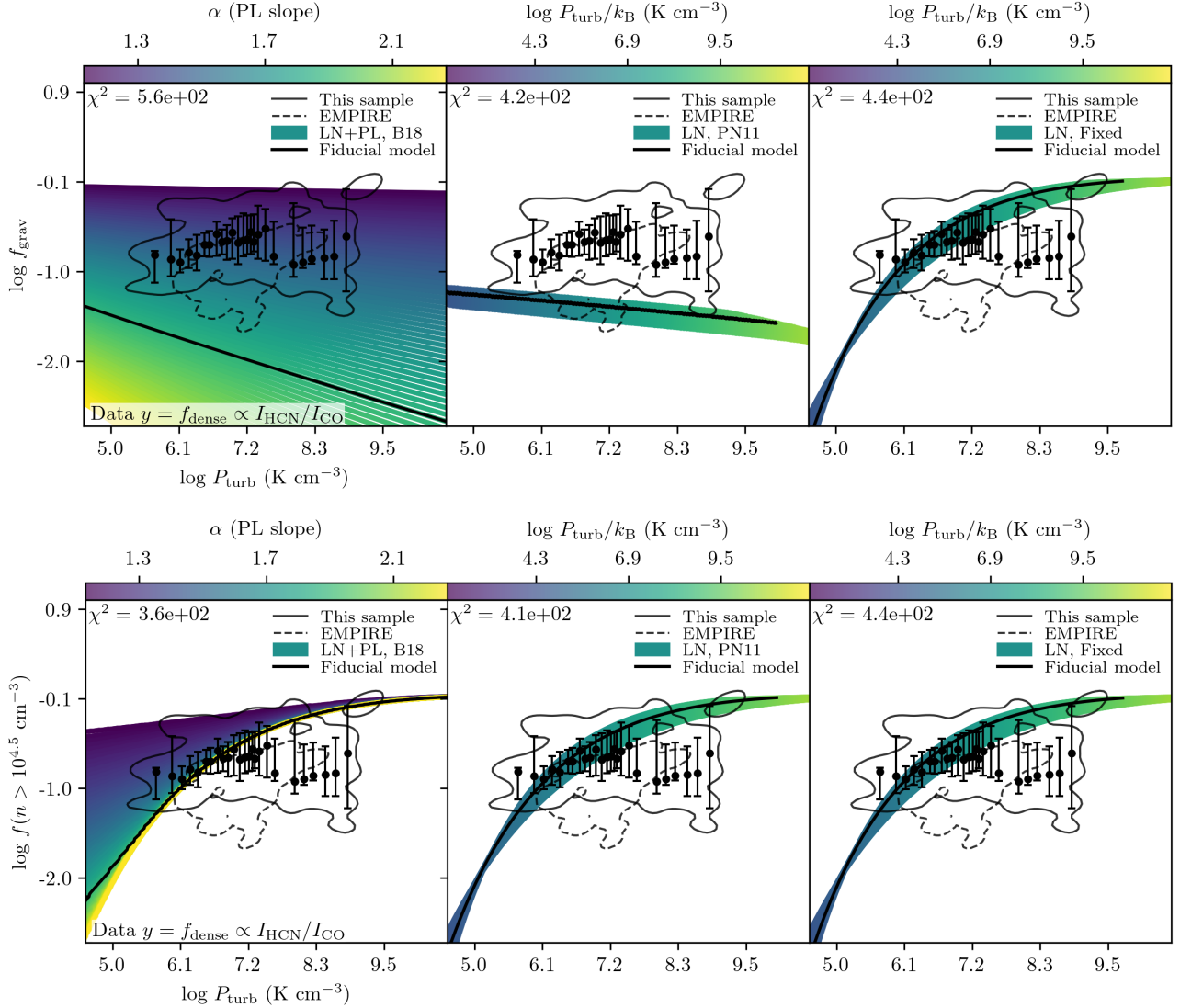


Figure 5. Model f_{grav} (top) and $f(n > 10^{4.5} \text{ cm}^{-3})$ (bottom) as a function of P_{turb} , compared to the data from our sample (solid black contours) and the EMPIRE sample (dashed black contours). Note that $f_{\text{grav}} \equiv f_{\text{dense}}$ for models with $n_{\text{SF}} = 10^{4.5} \text{ cm}^{-3}$. The LN+PL B18 models are colored by α_{PL} , and the LN models are colored by P_{turb} . χ^2 relative to the fiducial model is shown in the upper left corner of each plot. The median values of the data are shown with the black datapoints, and the errorbars correspond to the $1 - \sigma$ spread in each bin.

Model f_{grav} decreases with increasing P_{turb} for the models with varying thresholds (i.e. LN+PL B18 and LN P11, left two columns). f_{grav} predicted by the fixed-density threshold models is identical to $f(n > 10^{4.5} \text{ cm}^{-3})$ (right column) and increases with P_{turb} . Model $f(n > 10^{4.5} \text{ cm}^{-3})$ increases with P_{turb} for all models. From this result, the observed positive trend in $I_{\text{HCN}}/I_{\text{CO}}$ with P_{turb} is more consistent with $I_{\text{HCN}}/I_{\text{CO}}$ being a better tracer of $f(n > 10^{4.5} \text{ cm}^{-3})$ than f_{grav} .

trends observed with $f(n > 10^{4.5} \text{ cm}^{-3})$ for all models. f_{grav} is equivalent to $f(n > 10^{4.5} \text{ cm}^{-3})$ in the fixed-threshold models. From these results, the weak positive trend of $f_{\text{dense}} \propto I_{\text{HCN}}/I_{\text{CO}}$ with P_{turb} seen in our data is more consistent with the positive trend between $f(n > 10^{4.5} \text{ cm}^{-3})$ and P_{turb} seen in the models, and supports the conclusion that $I_{\text{HCN}}/I_{\text{CO}}$ is tracing gas above a roughly constant density but not necessar-

ily the f_{grav} predicted by gravoturbulent models of star formation.

4.2.1. The Star Formation Efficiency per Free-fall Time

As a check on the results above, we also consider ϵ_{ff} . In Fig. 6, we plot our data as a function of P_{turb} (left panel) and f_{dense} (right panel). In Fig. 7 we compare the model predictions of ϵ_{ff} with P_{turb} (top row), $f(n > 10^{4.5} \text{ cm}^{-3})$ (middle row), and f_{grav} (bottom row). ϵ_{ff} shows a weak negative correlation with P_{turb}

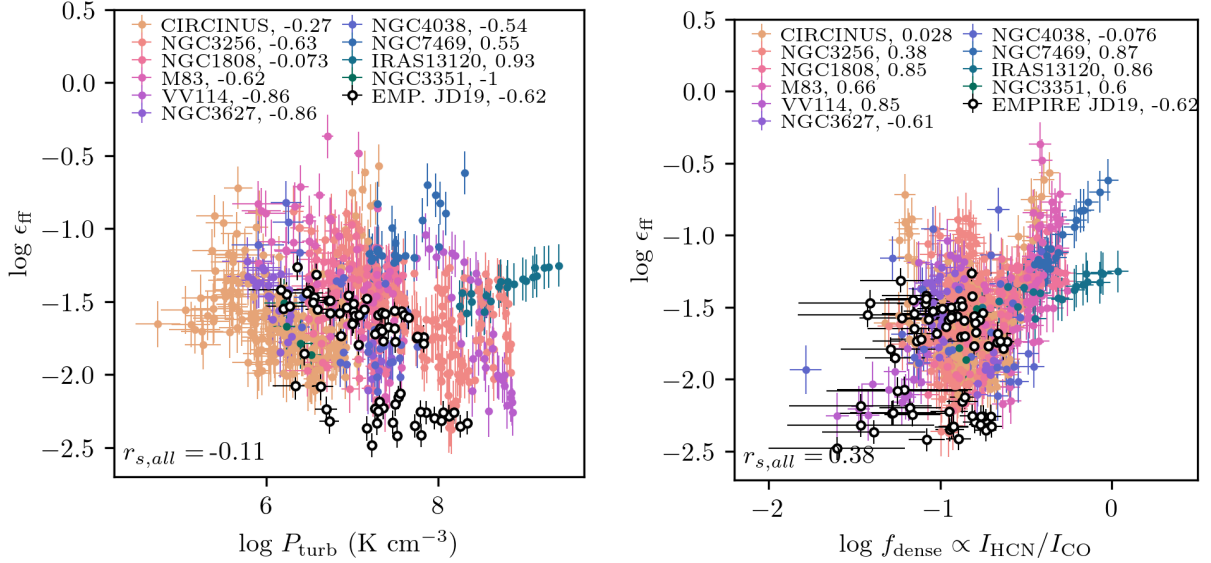


Figure 6. *Left:* The efficiency per free-fall time as a function of P_{turb} for our galaxies and the EMPIRE sample. Correlation coefficients are shown and data is colorized by galaxy, similar to the formatting in Fig. 2. The sample as a whole shows a weak, negative correlation between ϵ_{ff} and P_{turb} . The disk galaxies in the EMPIRE sample show a moderate, negative correlation. *Right:* The efficiency per free-fall time as a function of $f_{\text{dense}} \propto I_{\text{HCN}}/I_{\text{CO}}$. The sample as a whole shows a moderate, positive correlation between ϵ_{ff} and f_{dense} . The EMPIRE sample shows a moderate, negative correlation.

and a weak positive correlation with f_{dense} (Fig. 6) when considering our sample as a whole. These results are in agreement with the qualitative predictions of the varying density-threshold models (discussed in §3), where higher $\mathcal{M} \sim \sigma_v$ (and therefore $P_{\text{turb}} \sim \sigma_v^2$) yield a lower ϵ_{ff} .

1. *LN PN11:* The negative trend between ϵ_{ff} and P_{turb} seen in the data is not reproduced by the LN PN11 models (middle column, top row of Fig 7). However, the LN PN11 models do reproduce the positive between ϵ_{ff} and f_{dense} seen in the data when we consider $f(n > 10^{4.5} \text{ cm}^{-3})$ (middle row of Fig 7). There is some overlap between ϵ_{ff} and model f_{grav} (bottom row of Fig 7), but this trend does not track the positive relationship between ϵ_{ff} and f_{dense} seen in the data.
2. *LN+PL B18:* Similar to the LN PN11 models, the negative trend between ϵ_{ff} and P_{turb} seen in the data is not reproduced by any single value of α_{PL} for these models (left column, top row of Fig 7). Rather, the data overlap with these models for a range of α_{PL} , with higher values of ϵ_{ff} corresponding to lower values of α_{PL} and lower P_{turb} . Also similar to the LN PN11 models, the LN+PL B18 models do reproduce the positive trend between ϵ_{ff} and f_{dense} seen in the data when we consider $f(n > 10^{4.5} \text{ cm}^{-3})$ (middle row of Fig 7). In this case, the vertical spread in the data

corresponds to variations in α_{PL} . Models with lower α_{PL} also show an upturn in ϵ_{ff} at higher $f(n > 10^{4.5} \text{ cm}^{-3})$ consistent with the trend seen in the data.

At first look, the positive trend between ϵ_{ff} and f_{dense} seen in the data also appears consistent with the trend between ϵ_{ff} and model f_{grav} (bottom row of Fig 7). However, this requires that $f_{\text{dense}} \propto f_{\text{grav}}$, for which we find evidence to the contrary in the previous section.

3. *LN Fixed:* The fixed-threshold models predict an increase in ϵ_{ff} with P_{turb} up to $P_{\text{turb}} \approx 10^7 \text{ K cm}^{-3}$, after which this relationship flattens and ϵ_{ff} slightly turns over. This is not seen in our data. These models predict a positive relationship between ϵ_{ff} and f_{grav} up to $\log f_{\text{grav}} \approx -0.5$, above which ϵ_{ff} turns over. There is no evidence for this turnover in our data.

The varying threshold models are able to reproduce the positive trend seen between ϵ_{ff} and f_{dense} when considering $f(n > 10^{4.5} \text{ cm}^{-3})$. Some of the scatter is also reproduced by these models when considering a range in α_{PL} or a range in σ_v (cf. Fig. 7).

4.2.2. Total Gas Depletion Times

Now we consider if estimates of the total gas depletion times may give insight into the discrepancy between f_{grav} and observational estimates of f_{dense} . We

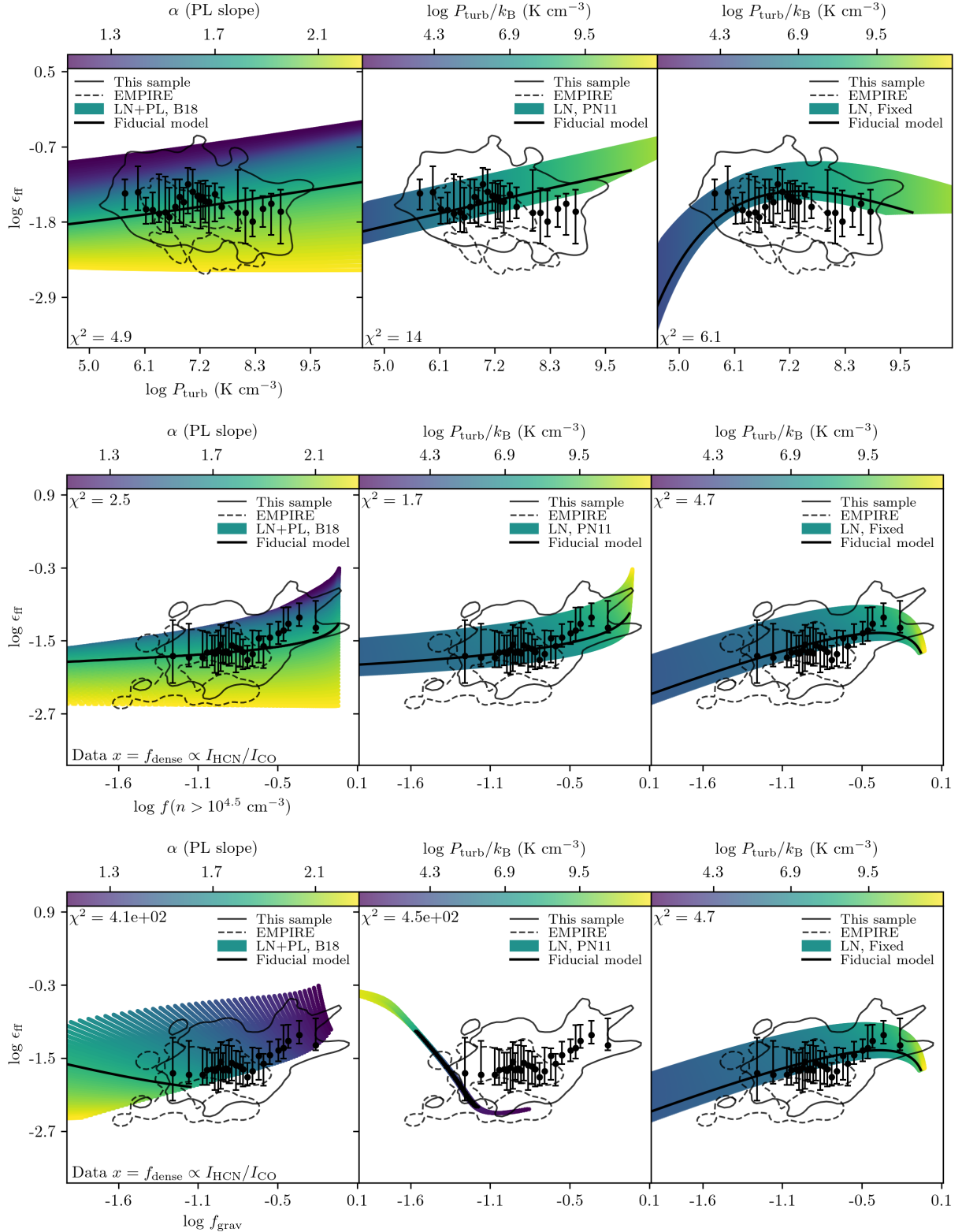


Figure 7. Model ϵ_{ff} as a function of P_{turb} (top), $f(n > 10^{4.5} \text{ cm}^{-3})$ (middle), and f_{grav} (bottom) compared to data from our sample (solid black contours) and the EMPIRE sample (dashed black contours). See Table 2 for information on how these values are calculated. The LN+PL B18 models are colored by α_{PL} , and the LN models are colored by P_{turb} . χ^2 relative to the fiducial model is shown in the bottom left corner of the plots in the top row, and the upper left corner of the plots in the bottom two rows. The median values of the data are shown with the black datapoints, and the errorbars correspond to the $1-\sigma$ spread in each bin. The bottom two rows show the importance of distinguishing f_{grav} from $f(n > 10^{4.5} \text{ cm}^{-3})$ when using $I_{\text{HCN}}/I_{\text{CO}}$ as a tracer of the dense, star forming gas. All models considered agree better with observations when using $f(n > 10^{4.5} \text{ cm}^{-3})$ as a proxy for the dense gas fraction traced by $I_{\text{HCN}}/I_{\text{CO}}$. Please see the text for a full analysis of the plots.

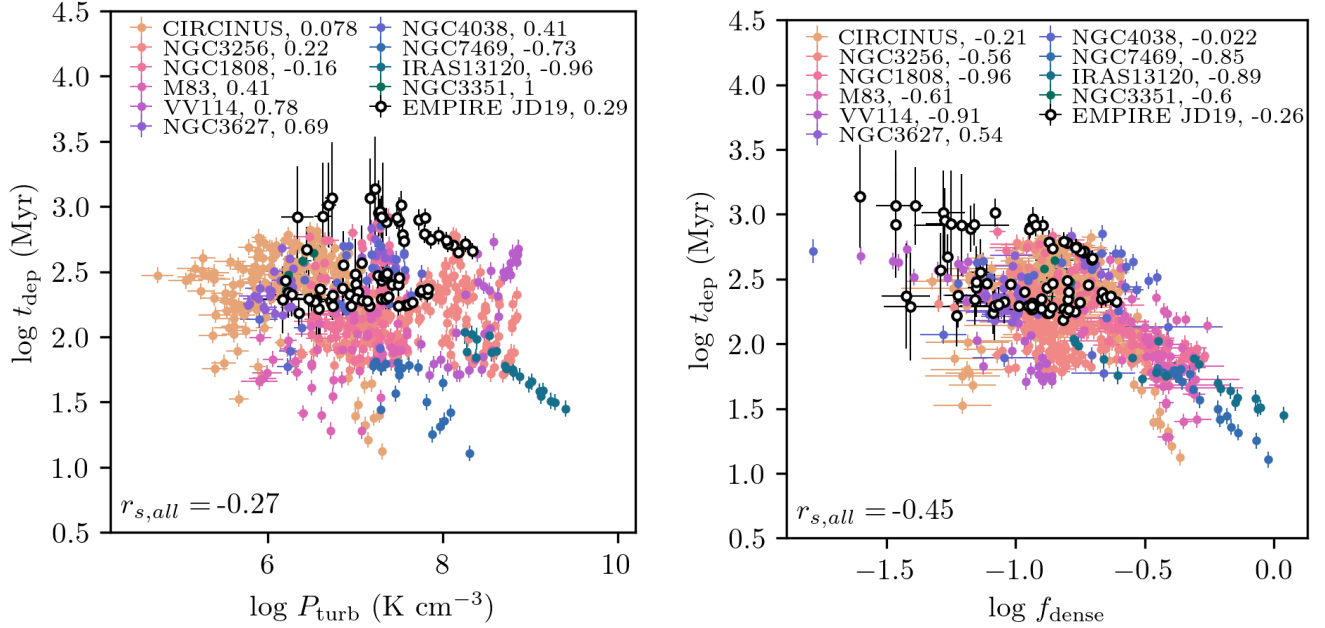


Figure 8. *Left:* Depletion time of the total molecular gas content as a function of P_{turb} for our galaxies and the EMPIRE sample. Correlation coefficients are shown and data is colored by galaxy, similar to the formatting in Fig. 2. The sample as a whole shows a weak, negative correlation between t_{dep} and P_{turb} . The disk galaxies in the EMPIRE sample show a weak, positive correlation. *Right:* Depletion time of the total molecular gas content as a function of f_{dense} (right). The sample as a whole shows a moderate, negative correlation between t_{dep} and P_{turb} . The disk galaxies in the EMPIRE sample show a weak, negative correlation. Data is formatted as it is in Fig 2.

plot t_{dep} as a function of P_{turb} and f_{dense} for our sample of galaxies in Fig. 8. We find moderate negative correlations between t_{dep} and the dense gas fraction traced by $I_{\text{HCN}}/I_{\text{CO}}$. t_{dep} estimated from the data appears relatively constant with P_{turb} , but the Spearman rank coefficient of the combined data indicates a moderate, negative correlation (cf. Fig. 8).

1. *LN PN11:* These models are able to reproduce the average trends seen in our data (i.e. negative trend between t_{dep} and P_{turb} and negative trend between t_{dep} and $f(n > 10^{4.5} \text{ cm}^{-3})$). Variations in P_{turb} alone do not reproduce the spread seen in our data. t_{dep} vs. f_{grav} does not track the relationship between t_{dep} and f_{dense} seen in the data.
2. *LN+PL B18:* We find good agreement between these models and the data when comparing t_{dep} , P_{turb} , and $f(n > 10^{4.5} \text{ cm}^{-3})$ (Fig. 9). Although the data overlap with t_{dep} vs. f_{grav} , the models show a much larger spread than that observed in the data.
3. *LN Fixed:* These models predict that t_{dep} decreases until $P_{\text{turb}} \sim 10^7 \text{ K cm}^{-3}$ until it reaches a roughly constant value. This behavior is not seen

in our data. t_{dep} monotonically decreases with $f(n > 10^{4.5} \text{ cm}^{-3})$ and f_{grav} for these models.

The varying-threshold models best reproduce the observed trend between t_{dep} and P_{turb} . The varying-threshold models also perform better than the fixed-threshold at reproducing the observed trend between t_{dep} and f_{dense} . Yet again, the trends in the data are best reproduced by the models when considering $f(n > 10^{4.5} \text{ cm}^{-3})$ rather than f_{grav} .

4.2.3. Dense Gas Depletion Times

We plot the depletion time of the dense gas as traced by HCN, $t_{\text{dep,dense}}$, as a function of P_{turb} (left) and dense gas fraction (right) in Fig. 10. We see a moderate positive correlation between $t_{\text{dep,dense}}$ and f_{dense} in ~ 3 of our sources and the EMPIRE galaxies. The Spearman rank coefficient shows a weak, positive correlation for the combined dataset. At first this appears counter to the expectation of star formation models, but all models except for those with a fixed threshold are able to roughly reproduce this increase in $t_{\text{dep,dense}}$ with gas fraction (cf. Fig. 11).

1. *LN PN11:* These models predict a turnover in $t_{\text{dep}}(n > 10^{4.5} \text{ cm}^{-3})$ with P_{turb} and in $t_{\text{dep}}(n > 10^{4.5} \text{ cm}^{-3})$ with $f(n > 10^{4.5} \text{ cm}^{-3})$ (cf. middle column, top and middle rows, respectively Fig.

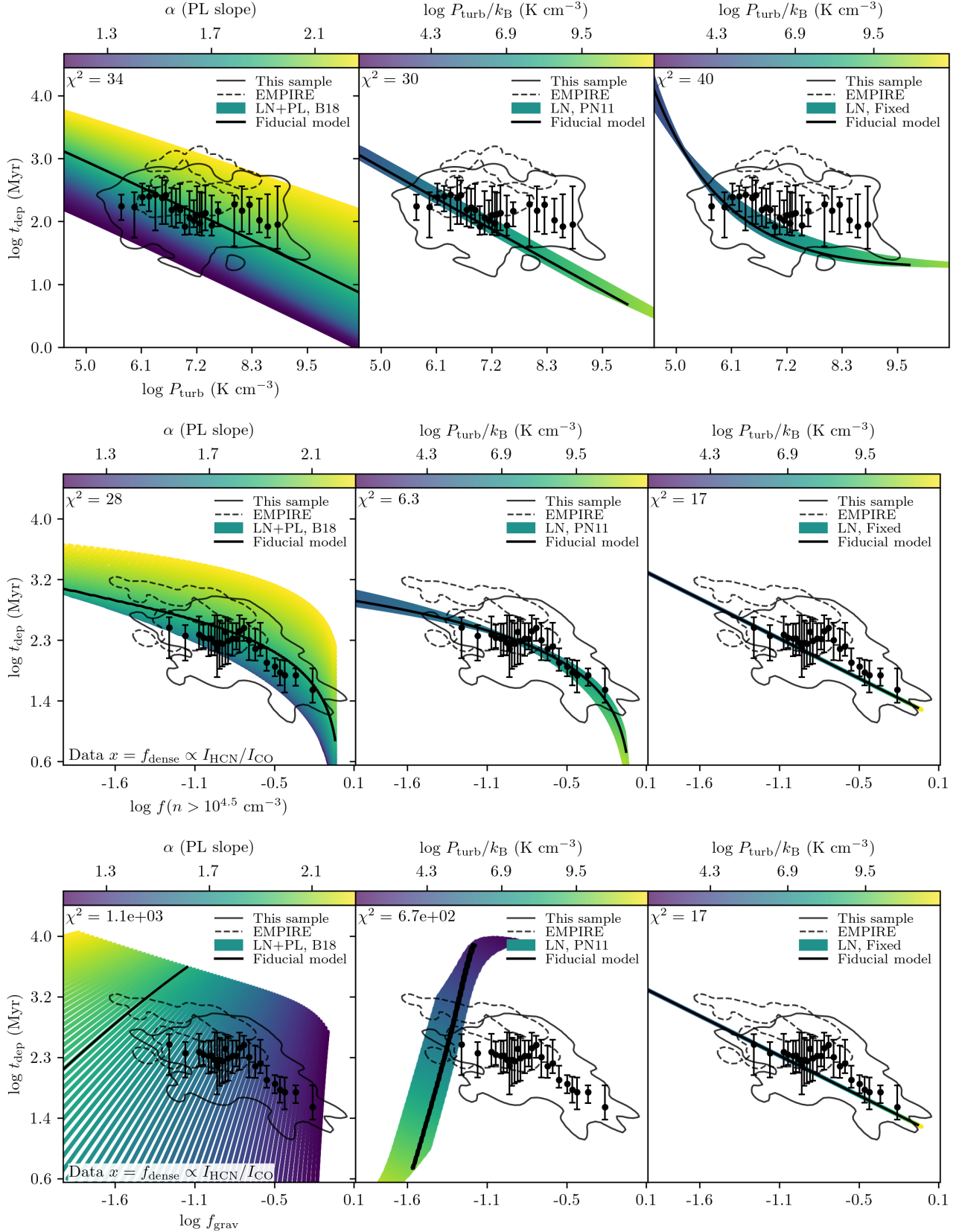


Figure 9. Model t_{dep} as a function of P_{turb} (top), $f(n > 10^{4.5} \text{ cm}^{-3})$ (middle), and f_{grav} (bottom) compared to the data from our sample (solid black contours) and the EMPIRE sample (dashed black contours). See Table 2 for information on how these values are calculated. The LN+PL B18 models are colored by α_{PL} , and the LN models are colored by P_{turb} . χ^2 relative to the fiducial model is shown in the upper left corner of each plot. The median values of the data are shown with the black datapoints, and the errorbars correspond to the $1 - \sigma$ spread in each bin. Similar to Fig. 7, the bottom two rows show the importance of distinguishing f_{grav} from $f(n > 10^{4.5} \text{ cm}^{-3})$ when using $I_{\text{HCN}}/I_{\text{CO}}$ as a tracer of the dense, star forming gas. All models considered agree better with observations when using $f(n > 10^{4.5} \text{ cm}^{-3})$ as a proxy for the dense gas fraction traced by $I_{\text{HCN}}/I_{\text{CO}}$. Please see the text for a full analysis of the plots.

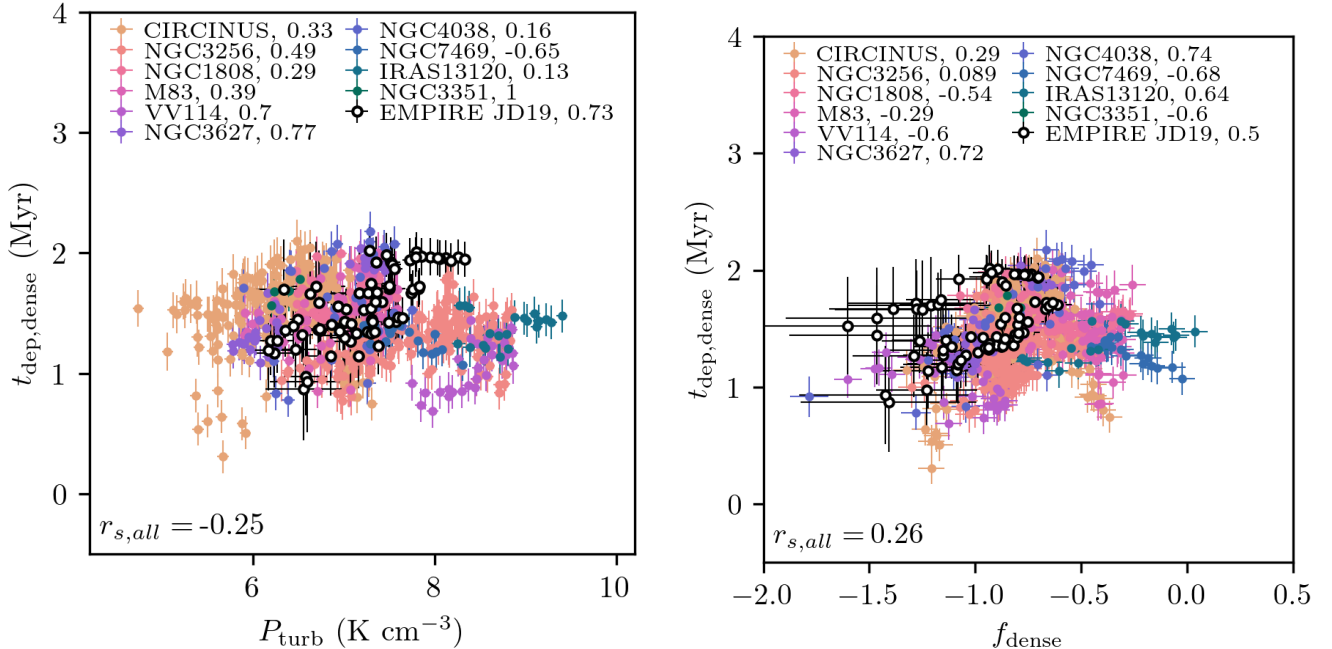


Figure 10. *Left:* Depletion time of the dense molecular gas content as a function of P_{turb} for our galaxies and the EMPIRE sample. Correlation coefficients are shown and data is colored by galaxy, similar to the formatting in Fig. 2. The sample as a whole shows a weak, negative correlation between $t_{\text{dep,dense}}$ and P_{turb} . The disk galaxies in the EMPIRE sample show a strong, positive correlation. *Right:* Depletion time of the dense molecular gas content as a function of f_{dense} (right). The sample as a whole shows a weak, positive correlation between t_{dep} and P_{turb} . The disk galaxies in the EMPIRE sample show a moderate, positive correlation. Data is formatted as it is in Fig 2.

- 11). This qualitatively agrees with the average trends seen in our data. We find that $t_{\text{dep,grav}}$ vs. f_{grav} does not track the relationship between t_{dep} and f_{dense} seen in the data. Variations in P_{turb} alone do not reproduce the spread seen in our data.
2. *LN+PL B18:* For $\alpha_{\text{PL}} > 1.7$, these models predict a turnover in $t_{\text{dep}}(n > 10^{4.5} \text{ cm}^{-3})$ around $P_{\text{turb}} \sim 10^7 \text{ K cm}^{-3}$ and for $\log f(n > 10^{4.5} \text{ cm}^{-3}) \sim -0.5$. For $\alpha_{\text{PL}} \leq 1.7$, $t_{\text{dep}}(n > 10^{4.5} \text{ cm}^{-3})$ consistently decreases with P_{turb} and $f(n > 10^{4.5} \text{ cm}^{-3})$. The observed trends in the data are in qualitative agreement with the trends seen for $\alpha_{\text{PL}} > 1.7$. We include $t_{\text{dep,grav}}$ vs. f_{grav} for completeness, but again find that the models show a much larger spread than that observed in the data.
3. *LN Fixed:* As predicted in §3.2, these models return a fixed $t_{\text{dep}}(n > 10^{4.5} \text{ cm}^{-3})$ regardless of variations in P_{turb} or $f(n > 10^{4.5} \text{ cm}^{-3})$.

The LN+PL B18 models are able to qualitatively reproduce the trends observed in $t_{\text{dep,dense}}$, P_{turb} , and f_{dense} for $\alpha_{\text{PL}} > 1.7$. The LN PN11 models are also able to reproduce the average trends, but variations in P_{turb} do not reproduce the observed scatter. The

above results again provide support against the interpretation of the $I_{\text{HCN}}/I_{\text{CO}}$ ratio as a tracer of f_{grav} . The observed trends are best reproduced by the varying-threshold models when considering $f(n > 10^{4.5}) \text{ cm}^{-3}$, but not with f_{grav} , and this is why our results provide support against this interpretation.

5. DISCUSSION

In this work, we explore how well the HCN-to-CO ratio is tracing the star forming fraction of gas in molecular clouds across the more extreme environments of U/LIRGs, mergers, and galaxy centers using gravo-turbulent models of star formation (Burkhart 2018; Burkhart & Mocz 2019; Padoan & Nordlund 2011; Krumholz & McKee 2005; Federrath & Klessen 2012; Hennebelle & Chabrier 2011). Previous studies find that HCN may be tracing gas above a fairly constant density and that the mass traced by HCN appears to scale linearly with the SFR, indicating a constant, average depletion time of the dense gas that spans clouds (cf. Wu et al. 2005) to entire galaxies including disk galaxies and U/LIRGs (cf. Gao & Solomon 2004a,b). This result is consistent with the predictions of the LN-only models with a fixed threshold that we consider in our analysis (see the right column of Figs. 3, 5, 7, 9, and 11). These models are able to qualitatively reproduce

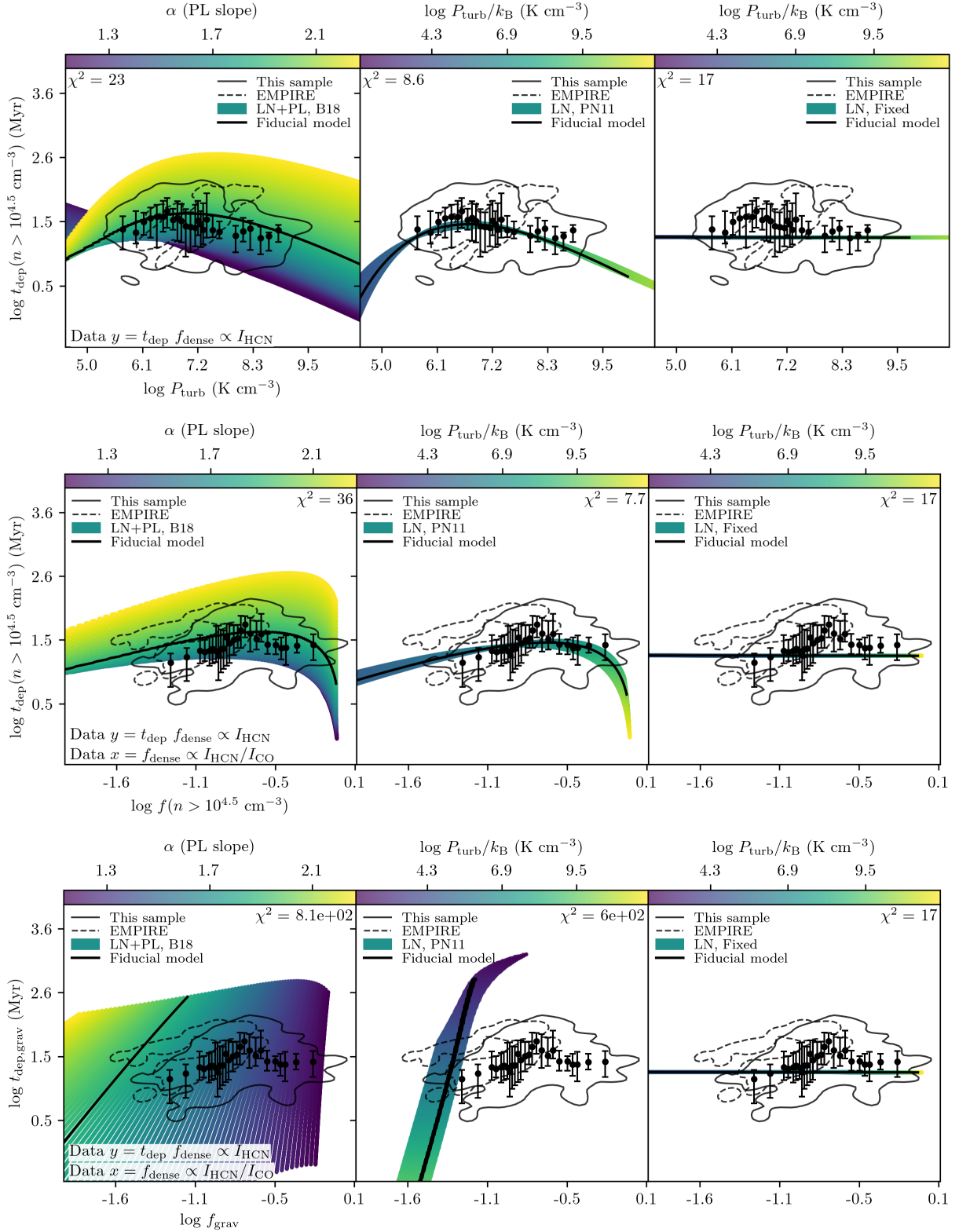


Figure 11. *Top two rows:* Depletion time of the molecular gas above $n = 10^{4.5} \text{ cm}^{-3}$ as a function of P_{turb} (top) and $f(n > 10^{4.5} \text{ cm}^{-3})$ (middle). *Bottom row:* Depletion time of the gravitationally-bound molecular gas as a function of f_{grav} . These trends are compared against our data (solid black contours) and the EMPIRE sample (dashed black contours). See Table 2 for information on how these values are calculated. The LN+PL B18 models are colored by α_{PL} , and the LN models are colored by P_{turb} . χ^2 relative to the fiducial model is shown in the upper left corner of the plots in the top row, and the upper right corner of the plots in the bottom two rows. The median values of the data are shown with the black datapoints, and the errorbars correspond to the $1 - \sigma$ spread in each bin. All models considered agree better with observations when using $f(n > 10^{4.5} \text{ cm}^{-3})$ as a proxy for the dense gas fraction traced by $I_{\text{HCN}}/I_{\text{CO}}$. Please see the text for a full analysis of the plots.

some of the average trends involving the dense, molecular gas traced by HCN such as the decrease in t_{dep} with increasing $f_{\text{dense}} \propto I_{\text{HCN}}/I_{\text{CO}}$ (Fig. 9). However, these models fail to capture the spread observed in many of the trends of our data and as well as the observed trends with P_{turb} .

The behavior of star formation laws observed in disk galaxies may give some insight into the discrepancy between the fixed-threshold models and observations. There is evidence of non-linear scalings between dense gas mass and the SFR within disk galaxies that appears to be correlated with galactic radius in disk galaxies (e.g. Gallagher et al. 2018; Usero et al. 2015; Chen et al. 2015). Relative to their disks, the centers of late-type galaxies show longer dense gas depletion times despite larger dense gas fractions traced by $I_{\text{HCN}}/I_{\text{CO}}$ (e.g. Gallagher et al. 2018; Usero et al. 2015; Chen et al. 2015). Similarly, the nuclei of the merging Antennae galaxies also display longer dense gas depletion times despite higher dense gas fractions compared to the Overlap region of this merging system (Bemis & Wilson 2019; Bigiel et al. 2015). Ambient pressure of the ISM is higher in the centers of disk galaxies compared to larger radii, which is apparent from observational estimates of P_{turb} from CO across the disks of nearby disk galaxies (cf. Gallagher et al. 2018). If higher P_{turb} is indicative of higher turbulent support, then gravoturbulent models of star formation with varying star formation thresholds may offer an explanation for these observed trends (i.e. Burkhart 2018; Padoan & Nordlund 2011; Krumholz & McKee 2005).

The varying-threshold models considered in this paper (i.e. Burkhart 2018; Padoan & Nordlund 2011) predict that the gas density required for the onset of collapse (and therefore star formation) increases in the presence of supportive processes such as solenoidal turbulence. This is apparent in Fig. 5 (left two columns, top row) where the LN+PL B18 and LN P11 models show a decrease in f_{grav} with increasing P_{turb} . Turbulence can also increase the mean gas density of the molecular cloud as a whole by widening the n -PDF. This is also apparent in Fig. 5 (left two columns, bottom row) where the LN+PL B18 and LN P11 models show an *increase* in $f(n > 10^{4.5} \text{ cm}^{-3})$ with increasing P_{turb} . The difference in behavior between f_{grav} and $f(n > 10^{4.5} \text{ cm}^{-3})$ with P_{turb} reflects an important prediction of these varying-threshold models: the supportive effect of turbulence can have a more significant impact on star formation than the increase in dense gas mass due to the widening of the n -PDF.

A wider n -PDF would naturally result in enhanced $I_{\text{HCN}}/I_{\text{CO}}$ if this ratio is tracing gas above a roughly con-

stant density (cf. Leroy et al. 2017a; Bemis 2020). At the same time, the star formation rate itself can appear suppressed relative to the total dense gas mass because the onset of star formation occurs at a higher density than the mean density of the gas traced by $I_{\text{HCN}}/I_{\text{CO}}$. The results of our work support this picture. In particular, the LN+PL B18 and LN P11 models are able to qualitatively reproduce the average trends observed in our data when considering $f(n > 10^{4.5} \text{ cm}^{-3})$ as a proxy for the dense gas fraction traced by $I_{\text{HCN}}/I_{\text{CO}}$ (cf. Figs. 5, 7, 9, and 11).

One apparent discrepancy between the data and the varying-threshold models is the behavior of ϵ_{ff} with P_{turb} (cf. top row, Fig. 7). Our sample shows a weak, negative trend between ϵ_{ff} and P_{turb} and the EMPIRE sample has a moderate, negative trend. Opposite to this, the varying-threshold models predict an increase in ϵ_{ff} with P_{turb} (cf. Fig. 7). The fixed-threshold LN model predicts that ϵ_{ff} initially increases with P_{turb} and then decreases towards higher pressures. The discrepancy between the models and data is likely in part due to inaccurate estimates of t_{ff} from our data. When estimating the mean density of the molecular gas traced by CO, we assume a fixed line-of-sight depth of 100 pc for all measurements, including those from the galaxies in the EMPIRE sample. We can also see from Fig. 9 that the models predict a steeper decline in t_{dep} with P_{turb} than what is observed in the data. These two things combined likely contribute to the discrepancy between the data and the models when considering ϵ_{ff} as a function of P_{turb} . Due to the weakness of the observed trend in our data and the uncertainty in t_{ff} , it is difficult to determine if ϵ_{ff} truly increases or decreases with P_{turb} . The apparent agreement between ϵ_{ff} and $f(n > 10^{4.5} \text{ cm}^{-3})$ predicted by the varying threshold models and our data may then be a reflection of the stronger connection between star formation and denser gas that is better traced by HCN relative to the bulk molecular gas traced by CO (cf. Gao & Solomon 2004a,b).

We also find that the scatter of the data is not well-reproduced by variations in P_{turb} when considering the LN-only models (e.g. Figs. 5, 7, 9, and 11). One parameter that we did not vary in this analysis is α_{vir} . We consider here how this would impact our results. For the Padoan & Nordlund (2011) models, higher α_{vir} increases n_{SF} such that more unbound clouds will have lower ϵ_{ff} . Variations in α_{vir} would introduce some scatter into the results, primarily in the relationships that depend on ϵ_{ff} and t_{dep} . However, variations in \mathcal{M} have an impact on both the width of the n -PDF (Eq. 17) and the shift in n_{SF} (Eq. 19) for the LN PN11 models, while changes in α_{vir} primarily have an impact on n_{SF} . Changes in the

dense gas fraction indicated by $f(n > 10^{4.5} \text{ cm}^{-3})$ are not analytically dependent on α_{vir} , and therefore would need an additional explanation.

The LN+PL B18 models offer an alternative explanation for the scatter of the data: variations in PL slope (α_{PL}). Simulations show that a PL tail develops as a consequence of cloud evolution as gas becomes self-gravitating, and the slope of the PL tail becomes more shallow as the fraction of bound gas (i.e. f_{grav}) increases (cf. Ballesteros-Paredes et al. 2011; Collins et al. 2012; Schneider et al. 2015; Burkhart et al. 2017; Padoan et al. 2017). This is supported by observations of some Milky Way clouds which show a PL tail at high densities (e.g. Kainulainen et al. 2009; Schneider et al. 2013; Lombardi et al. 2015; Schneider et al. 2015, 2016; Alves et al. 2017). Additionally, there is observational evidence for a connection between PL slope and ϵ_{ff} which matches the predictions of the LN+PL B18 models (Burkhart & Mocz 2019; Federrath & Klessen 2013).

The scatter in our data is well-reproduced for $\alpha_{\text{PL}} = 1 - 2.3$ (see the left column of Figs. 3, 5, 7, 9, and 11). These models are also able to reproduce the average trends of our data. Out of the three models we consider, the LN+PL B18 models perform best at reproducing the observational trends and scatter of our data and the EMPIRE sample. In the context of the LN+PL B18 models, the scatter in our data is therefore driven in part due to cloud evolution (Ballesteros-Paredes et al. 2011), such that the n -PDF of clouds evolves from a lognormal shape to a composite lognormal and powerlaw over time as more gas becomes gravitationally-bound. The underlying trends are still driven largely by variations in turbulence, which we impose in our model parameter space by using the observational relationship between gas surface density and velocity dispersion found by Sun et al. (2018) (cf. Eq. 24).

6. CONCLUSIONS

We find the following conclusions from our comparison between observation and the predictions of analytical models of star formation:

1. KS relationship: For the model parameter space considered, none of the models reproduce the multi-slope KS relationship as found in Wilson et al. (2019). Variations in the slope of the $\Sigma_{\text{mol}} - \sigma_v$ relationship can produce variations in the KS slope, such that a shallower (steeper) $\Sigma_{\text{mol}} - \sigma_v$ relationship would produce a shallower (steeper) KS relationship. Furthermore, systematic changes in ϵ_0 or PL slope with Σ_{mol} could also affect the KS slope. Increasing (decreasing) PL slope with Σ_{mol} would produce a shallower (steeper) KS rela-

tionship. Similarly, decreasing (increasing) ϵ_0 with Σ_{mol} produces a shallower (steeper) KS slope.

2. f_{dense} and f_{grav} : For the PN11 and B18 models, f_{grav} decreases with P_{turb} , and increases for the fixed-threshold models. $f(n > 10^{4.5} \text{ cm}^{-3})$ increases with P_{turb} for all models. The behavior of $f(n > 10^{4.5} \text{ cm}^{-3})$ with P_{turb} is in qualitative agreement with our data, which shows an increase in $f_{\text{dense}} = (\alpha_{\text{HCN}}/\alpha_{\text{CO}})I_{\text{HCN}}/I_{\text{CO}}$ with observational estimates of P_{turb} . We therefore conclude that the $I_{\text{HCN}}/I_{\text{CO}}$ ratio likely does not track f_{grav} as predicted by the varying-threshold models, but rather the fraction of gas above some fixed density, such as $f(n > 10^{4.5} \text{ cm}^{-3})$.
3. ϵ_{ff} : For the PN11 and B18 models, ϵ_{ff} increases with P_{turb} on average. For the fixed-threshold models, ϵ_{ff} increases with P_{turb} until $P_{\text{turb}}/k_{\text{B}} \approx 10^{7.5} \text{ K cm}^{-3}$ where it turns over. All models predict an increase in ϵ_{ff} with $f(n > 10^{4.5} \text{ cm}^{-3})$, on average, with only the fixed-threshold models showing a turnover in this relationship at high fractions. ϵ_{ff} decreases with f_{grav} for the the PN11 models and the B18 models for fixed α_{PL} . For the fixed-threshold models, ϵ_{ff} increases with f_{grav} until it turns over at high fractions. Under the assumption of a fixed l.o.s. depth, our data show a weak decrease in ϵ_{ff} with P_{turb} and increase with f_{dense} . This is in qualitative agreement with the PN11 and B18 models, assuming $I_{\text{HCN}}/I_{\text{CO}}$ is tracking $f(n > 10^{4.5} \text{ cm}^{-3})$, but not f_{grav} .
4. Total gas depletion time: All models predict a decrease of t_{dep} with both P_{turb} and $f(n > 10^{4.5} \text{ cm}^{-3})$. The fixed-threshold models predict a flattening of t_{dep} with higher P_{turb} but a constant decrease with $f(n > 10^{4.5} \text{ cm}^{-3})$. Contrary to this, the PN11 models and the B18 models show a constant decrease in t_{dep} with P_{turb} , but a steepening decline in t_{dep} with higher $f(n > 10^{4.5} \text{ cm}^{-3})$. t_{dep} increases with f_{grav} for the PN11 models and the B18 models for fixed α_{PL} . The trends in data are in better qualitative agreement with the PN11 and B18 models, again assuming $I_{\text{HCN}}/I_{\text{CO}}$ is tracking $f(n > 10^{4.5} \text{ cm}^{-3})$, but not f_{grav} .
5. Dense gas depletion time: The PN11 and B18 models (for $\alpha_{\text{PL}} > 1.7$) predict a turnover in the depletion time of dense gas, $t_{\text{dep}}(n > 10^{4.5} \text{ cm}^{-3})$, with P_{turb} and $f(n > 10^{4.5} \text{ cm}^{-3})$, while the fixed threshold models predict a constant dense gas depletion time (Gao & Solomon 2004a,b). We note that $\alpha_{\text{PL}} < 1.7$ produce a nearly constant decrease

in $t_{\text{dep}}(n > 10^{4.5} \text{ cm}^{-3})$ with P_{turb} and $f(n > 10^{4.5} \text{ cm}^{-3})$. $t_{\text{dep,grav}}$ increases with f_{grav} for the PN11 models and the B18 models for fixed α_{PL} . The trends in data are in better qualitative agreement with the PN11 and B18 models, again assuming $I_{\text{HCN}}/I_{\text{CO}}$ is tracking $f(n > 10^{4.5} \text{ cm}^{-3})$, but not f_{grav} .

6. Variations in PL slope (α_{PL}) (lognormal+powerlaw B18 models) are able to explain the scatter in the data. The scatter in our data is not well-reproduced by variations in P_{turb} (or \mathcal{M}) alone.
7. The varying-threshold models (lognormal+powerlaw B18 and lognormal-only PN11) are able to better reproduce the average trends of our data and the EMPIRE sample compared to the fixed-threshold lognormal-only models.
8. The average trends in the data with P_{turb} and f_{dense} are likely set by variations in turbulence determined by local environment within each galaxy.

In summary, the HCN/CO ratio is likely a reliable tracer of gas above a constant density, such as $n_{\text{SF}} \approx 10^{4.5} \text{ cm}^{-3}$, but not necessarily f_{grav} . If varying thresholds for star forming gas exist in nature, then the HCN/CO ratio is a poor tracer of f_{grav} .

7. ACKNOWLEDGEMENTS

This paper makes use of the following ALMA data: ADS/JAO.ALMA#2011.0.00467.S, ADS/JAO.ALMA#2011.0.00525.S, ADS/JAO.ALMA#2011.0.00772.S, ADS/JAO.ALMA#2012.1.00165.S, ADS/JAO.ALMA#2012.1.00185.S, ADS/JAO.ALMA#2012.1.01004.S, ADS/JAO.ALMA#2013.1.00218.S, ADS/JAO.ALMA#2013.1.00247.S, ADS/JAO.ALMA#2013.1.00634.S, ADS/JAO.ALMA#2013.1.00885.S, ADS/JAO.ALMA#2013.1.00911.S, ADS/JAO.ALMA#2013.1.01057.S, ADS/JAO.ALMA#2015.1.00993.S, ADS/JAO.ALMA#2015.1.01177.S, ADS/JAO.ALMA#2015.1.01286.S, ADS/JAO.ALMA#2015.1.01538.S. ALMA is a partnership of ESO (representing its member states), NSF (USA) and NINS (Japan), together with NRC (Canada), MOST and ASIAA (Taiwan), and KASI (Republic of Korea), in cooperation with the Republic of Chile. The Joint ALMA Observatory is operated by ESO, AUI/NRAO and NAOJ.

Software: This work made use of the following software packages: ASTROPY (Astropy Collaboration et al. 2013, 2018, 2022), CASA (McMullin et al. 2007), CMASHER (?), MATPLOTLIB (?), NUMPY (?), SCIPY (?), SPECTRAL-CUBE (<https://spectral-cube.readthedocs.io/en/latest/>).

APPENDIX

A. APPENDIX: MOMENT MAPS AND UNCERTAINTIES

We use the following expressions to calculate moments and their corresponding uncertainties.

$$\text{MOMENT 0 : } I = \Sigma_i T_i \Delta v \quad (\text{A1})$$

$$\delta I = \delta \bar{T} \Delta v \sqrt{N_{\text{chan}}} \quad (\text{A2})$$

$$\text{MOMENT 1 : } \bar{v} = \frac{\Sigma_i T_i v_i}{\Sigma_i T_i} \quad (\text{A3})$$

$$\delta \bar{v} = \frac{N_{\text{chan}} \Delta v}{2\sqrt{3}} \frac{\delta I}{I} \quad (\text{A4})$$

$$\text{MOMENT 2 : } \sigma_v = \sqrt{\frac{\Sigma_i T_i (v_i - \bar{v})^2}{\Sigma_i T_i}} \quad (\text{A5})$$

$$\delta \sigma_v = \frac{\delta I}{I} \frac{(N_{\text{chan}} \Delta v)^2}{8\sqrt{5}} \frac{1}{\sigma_v} \quad (\text{A6})$$

A full derivation of the uncertainties on Eqs. A4 and A6 is given in Wilson et al. (submitted).

REFERENCES

- Alves, J., Lombardi, M., & Lada, C. J. 2017, *A&A*, 606, L2, doi: [10.1051/0004-6361/201731436](https://doi.org/10.1051/0004-6361/201731436)
- André, P., Revéret, V., Könyves, V., et al. 2016, *A&A*, 592, A54, doi: [10.1051/0004-6361/201628378](https://doi.org/10.1051/0004-6361/201628378)
- Aniano, G., Draine, B. T., Gordon, K. D., & Sandstrom, K. 2011, *PASP*, 123, 1218, doi: [10.1086/662219](https://doi.org/10.1086/662219)
- Astropy Collaboration, Robitaille, T. P., Tollerud, E. J., et al. 2013, *A&A*, 558, A33, doi: [10.1051/0004-6361/201322068](https://doi.org/10.1051/0004-6361/201322068)
- Astropy Collaboration, Price-Whelan, A. M., Sipőcz, B. M., et al. 2018, *AJ*, 156, 123, doi: [10.3847/1538-3881/aabc4f](https://doi.org/10.3847/1538-3881/aabc4f)
- Astropy Collaboration, Price-Whelan, A. M., Lim, P. L., et al. 2022, *ApJ*, 935, 167, doi: [10.3847/1538-4357/ac7c74](https://doi.org/10.3847/1538-4357/ac7c74)
- Ballesteros-Paredes, J., Vázquez-Semadeni, E., Gazol, A., et al. 2011, *MNRAS*, 416, 1436, doi: [10.1111/j.1365-2966.2011.19141.x](https://doi.org/10.1111/j.1365-2966.2011.19141.x)
- Bemis, A., & Wilson, C. D. 2019, *AJ*, 157, 131, doi: [10.3847/1538-3881/ab041d](https://doi.org/10.3847/1538-3881/ab041d)
- Bemis, a. R. 2020, PhD thesis, McMaster University. <http://hdl.handle.net/11375/26061>
- Berkhuijsen, E. M., & Fletcher, A. 2008, *MNRAS*, 390, L19, doi: [10.1111/j.1745-3933.2008.00526.x](https://doi.org/10.1111/j.1745-3933.2008.00526.x)
- Bigiel, F., Leroy, A., Walter, F., et al. 2008, *AJ*, 136, 2846, doi: [10.1088/0004-6256/136/6/2846](https://doi.org/10.1088/0004-6256/136/6/2846)
- Bigiel, F., Leroy, A. K., Blitz, L., et al. 2015, *ApJ*, 815, 103, doi: [10.1088/0004-637X/815/2/103](https://doi.org/10.1088/0004-637X/815/2/103)
- Bolatto, A. D., Wolfire, M., & Leroy, A. K. 2013, *ARAA*, 51, 207, doi: [10.1146/annurev-astro-082812-140944](https://doi.org/10.1146/annurev-astro-082812-140944)
- Brunetti, N., Wilson, C. D., Sliwa, K., et al. 2021, *MNRAS*, 500, 4730, doi: [10.1093/mnras/staa3425](https://doi.org/10.1093/mnras/staa3425)
- Brunt, C. M., Federrath, C., & Price, D. J. 2010, *MNRAS*, 405, L56, doi: [10.1111/j.1745-3933.2010.00858.x](https://doi.org/10.1111/j.1745-3933.2010.00858.x)
- Burkhart, B. 2018, *ApJ*, 863, 118, doi: [10.3847/1538-4357/aad002](https://doi.org/10.3847/1538-4357/aad002)
- Burkhart, B., & Lazarian, A. 2012, *ApJL*, 755, L19, doi: [10.1088/2041-8205/755/1/L19](https://doi.org/10.1088/2041-8205/755/1/L19)
- Burkhart, B., Lee, M.-Y., Murray, C. E., & Stanimirović, S. 2015, *ApJL*, 811, L28, doi: [10.1088/2041-8205/811/2/L28](https://doi.org/10.1088/2041-8205/811/2/L28)
- Burkhart, B., & Mocz, P. 2019, *ApJ*, 879, 129, doi: [10.3847/1538-4357/ab25ed](https://doi.org/10.3847/1538-4357/ab25ed)
- Burkhart, B., Ossenkopf, V., Lazarian, A., & Stutzki, J. 2013, *ApJ*, 771, 122, doi: [10.1088/0004-637X/771/2/122](https://doi.org/10.1088/0004-637X/771/2/122)
- Burkhart, B., Stalpes, K., & Collins, D. C. 2017, *ApJL*, 834, L1, doi: [10.3847/2041-8213/834/1/L1](https://doi.org/10.3847/2041-8213/834/1/L1)
- Chen, H., Gao, Y., Braine, J., & Gu, Q. 2015, *ApJ*, 810, 140, doi: [10.1088/0004-637X/810/2/140](https://doi.org/10.1088/0004-637X/810/2/140)
- Chen, H. H.-H., Burkhart, B., Goodman, A., & Collins, D. C. 2018, *ApJ*, 859, 162, doi: [10.3847/1538-4357/aabaf6](https://doi.org/10.3847/1538-4357/aabaf6)

- Chevance, M., Madden, S. C., Fischer, C., et al. 2020, *MNRAS*, 494, 5279, doi: [10.1093/mnras/staa1106](https://doi.org/10.1093/mnras/staa1106)
- Collins, D. C., Kritsuk, A. G., Padoan, P., et al. 2012, *ApJ*, 750, 13, doi: [10.1088/0004-637X/750/1/13](https://doi.org/10.1088/0004-637X/750/1/13)
- Downes, D., Solomon, P. M., & Radford, S. J. E. 1993, *ApJl*, 414, L13, doi: [10.1086/186984](https://doi.org/10.1086/186984)
- Draine, B. 2010, *Physics of the Interstellar and Intergalactic Medium*, Princeton Series in Astrophysics (Princeton University Press).
<https://books.google.ca/books?id=FycJvKHYiwsC>
- Evans, Neal J., I., Dunham, M. M., Jørgensen, J. K., et al. 2009, *ApJS*, 181, 321, doi: [10.1088/0067-0049/181/2/321](https://doi.org/10.1088/0067-0049/181/2/321)
- Federrath, C., & Banerjee, S. 2015, *MNRAS*, 448, 3297, doi: [10.1093/mnras/stv180](https://doi.org/10.1093/mnras/stv180)
- Federrath, C., & Klessen, R. S. 2012, *ApJ*, 761, 156, doi: [10.1088/0004-637X/761/2/156](https://doi.org/10.1088/0004-637X/761/2/156)
- . 2013, *ApJ*, 763, 51, doi: [10.1088/0004-637X/763/1/51](https://doi.org/10.1088/0004-637X/763/1/51)
- Gallagher, M. J., Leroy, A. K., Bigiel, F., et al. 2018, *ApJ*, 858, 90, doi: [10.3847/1538-4357/aabad8](https://doi.org/10.3847/1538-4357/aabad8)
- Gao, Y., & Solomon, P. M. 2004a, *ApJS*, 152, 63, doi: [10.1086/383003](https://doi.org/10.1086/383003)
- . 2004b, *ApJ*, 606, 271, doi: [10.1086/382999](https://doi.org/10.1086/382999)
- Ginsburg, A., Koch, E., Robitaille, T., et al. 2019, *radio-astro-tools/spectral-cube: Release v0.4.5, v0.4.5*, Zenodo, Zenodo, doi: [10.5281/zenodo.3558614](https://doi.org/10.5281/zenodo.3558614)
- Goodman, A. A., Pineda, J. E., & Schnee, S. L. 2009, *ApJ*, 692, 91, doi: [10.1088/0004-637X/692/1/91](https://doi.org/10.1088/0004-637X/692/1/91)
- Grenier, I. A., Casandjian, J.-M., & Terrier, R. 2005, *Science*, 307, 1292, doi: [10.1126/science.1106924](https://doi.org/10.1126/science.1106924)
- Grudić, M. Y., Hopkins, P. F., Faucher-Giguère, C.-A., et al. 2018, *MNRAS*, 475, 3511, doi: [10.1093/mnras/sty035](https://doi.org/10.1093/mnras/sty035)
- Helfer, T. T., & Blitz, L. 1997a, *ApJ*, 478, 162, doi: [10.1086/303760](https://doi.org/10.1086/303760)
- . 1997b, *ApJ*, 478, 233, doi: [10.1086/303774](https://doi.org/10.1086/303774)
- Hennabelle, P., & Chabrier, G. 2011, *ApJl*, 743, L29, doi: [10.1088/2041-8205/743/2/L29](https://doi.org/10.1088/2041-8205/743/2/L29)
- Heyer, M., Krawczyk, C., Duval, J., & Jackson, J. M. 2009, *ApJ*, 699, 1092, doi: [10.1088/0004-637X/699/2/1092](https://doi.org/10.1088/0004-637X/699/2/1092)
- Hill, A. S., Benjamin, R. A., Kowal, G., et al. 2008, *ApJ*, 686, 363, doi: [10.1086/590543](https://doi.org/10.1086/590543)
- Imara, N., & Burkhart, B. 2016, *ApJ*, 829, 102, doi: [10.3847/0004-637X/829/2/102](https://doi.org/10.3847/0004-637X/829/2/102)
- Jameson, K. E., Bolatto, A. D., Wolfire, M., et al. 2018, *ApJ*, 853, 111, doi: [10.3847/1538-4357/aaa4bb](https://doi.org/10.3847/1538-4357/aaa4bb)
- Jarrett, T. H., Chester, T., Cutri, R., Schneider, S. E., & Huchra, J. P. 2003, *AJ*, 125, 525, doi: [10.1086/345794](https://doi.org/10.1086/345794)
- Jiménez-Donaire, M. J., Bigiel, F., Leroy, A. K., et al. 2019, *ApJ*, 880, 127, doi: [10.3847/1538-4357/ab2b95](https://doi.org/10.3847/1538-4357/ab2b95)
- Kainulainen, J., Beuther, H., Henning, T., & Plume, R. 2009, *A&A*, 508, L35, doi: [10.1051/0004-6361/200913605](https://doi.org/10.1051/0004-6361/200913605)
- Kainulainen, J., & Federrath, C. 2017, *A&A*, 608, L3, doi: [10.1051/0004-6361/201731028](https://doi.org/10.1051/0004-6361/201731028)
- Kainulainen, J., & Tan, J. C. 2013, *A&A*, 549, A53, doi: [10.1051/0004-6361/201219526](https://doi.org/10.1051/0004-6361/201219526)
- Kauffmann, J., Bertoldi, F., Bourke, T. L., Evans, N. J., I., & Lee, C. W. 2008, *A&A*, 487, 993, doi: [10.1051/0004-6361:200809481](https://doi.org/10.1051/0004-6361:200809481)
- Kauffmann, J., Goldsmith, P. F., Melnick, G., et al. 2017, *A&A*, 605, L5, doi: [10.1051/0004-6361/201731123](https://doi.org/10.1051/0004-6361/201731123)
- Kennicutt, Robert C., J., & De Los Reyes, M. A. C. 2021, *ApJ*, 908, 61, doi: [10.3847/1538-4357/abd3a2](https://doi.org/10.3847/1538-4357/abd3a2)
- Kim, C.-G., Kim, W.-T., & Ostriker, E. C. 2011, *ApJ*, 743, 25, doi: [10.1088/0004-637X/743/1/25](https://doi.org/10.1088/0004-637X/743/1/25)
- Kim, W.-T., & Ostriker, E. C. 2002, *ApJ*, 570, 132, doi: [10.1086/339352](https://doi.org/10.1086/339352)
- Krumholz, M. R. 2014, *Phys. Rep.*, 539, 49, doi: [10.1016/j.physrep.2014.02.001](https://doi.org/10.1016/j.physrep.2014.02.001)
- Krumholz, M. R., Dekel, A., & McKee, C. F. 2012, *ApJ*, 745, 69, doi: [10.1088/0004-637X/745/1/69](https://doi.org/10.1088/0004-637X/745/1/69)
- Krumholz, M. R., & McKee, C. F. 2005, *ApJ*, 630, 250, doi: [10.1086/431734](https://doi.org/10.1086/431734)
- Lada, C. J., Lada, E. A., Clemens, D. P., & Bally, J. 1994, *ApJ*, 429, 694, doi: [10.1086/174354](https://doi.org/10.1086/174354)
- Lada, C. J., Lombardi, M., & Alves, J. F. 2010, *ApJ*, 724, 687, doi: [10.1088/0004-637X/724/1/687](https://doi.org/10.1088/0004-637X/724/1/687)
- Lada, E. A., Bally, J., & Stark, A. A. 1991a, *ApJ*, 368, 432, doi: [10.1086/169708](https://doi.org/10.1086/169708)
- Lada, E. A., Depoy, D. L., Evans, Neal J., I., & Gatley, I. 1991b, *ApJ*, 371, 171, doi: [10.1086/169881](https://doi.org/10.1086/169881)
- Langer, W. D., Velusamy, T., Pineda, J. L., Willacy, K., & Goldsmith, P. F. 2014, *A&A*, 561, A122, doi: [10.1051/0004-6361/201322406](https://doi.org/10.1051/0004-6361/201322406)
- Larson, R. B. 1981, *MNRAS*, 194, 809, doi: [10.1093/mnras/194.4.809](https://doi.org/10.1093/mnras/194.4.809)
- Lee, E. J., Miville-Deschênes, M.-A., & Murray, N. W. 2016, *ApJ*, 833, 229, doi: [10.3847/1538-4357/833/2/229](https://doi.org/10.3847/1538-4357/833/2/229)
- Leroy, A. K., Usero, A., Schrubba, A., et al. 2017a, *ApJ*, 835, 217, doi: [10.3847/1538-4357/835/2/217](https://doi.org/10.3847/1538-4357/835/2/217)
- Leroy, A. K., Schinnerer, E., Hughes, A., et al. 2017b, *ApJ*, 846, 71, doi: [10.3847/1538-4357/aa7fef](https://doi.org/10.3847/1538-4357/aa7fef)
- Lombardi, M., Alves, J., & Lada, C. J. 2015, *A&A*, 576, L1, doi: [10.1051/0004-6361/201525650](https://doi.org/10.1051/0004-6361/201525650)
- McKee, C. F., & Ostriker, E. C. 2007, *ARAA*, 45, 565, doi: [10.1146/annurev.astro.45.051806.110602](https://doi.org/10.1146/annurev.astro.45.051806.110602)

- McMullin, J. P., Waters, B., Schiebel, D., Young, W., & Golap, K. 2007, in *Astronomical Society of the Pacific Conference Series*, Vol. 376, *Astronomical Data Analysis Software and Systems XVI*, ed. R. A. Shaw, F. Hill, & D. J. Bell, 127
- Molina, F. Z., Glover, S. C. O., Federrath, C., & Klessen, R. S. 2012, *MNRAS*, 423, 2680, doi: [10.1111/j.1365-2966.2012.21075.x](https://doi.org/10.1111/j.1365-2966.2012.21075.x)
- Murphy, E. J., Condon, J. J., Schinnerer, E., et al. 2011, *ApJ*, 737, 67, doi: [10.1088/0004-637X/737/2/67](https://doi.org/10.1088/0004-637X/737/2/67)
- Nordlund, Å. K., & Padoan, P. 1999, in *Interstellar Turbulence*, ed. J. Franco & A. Carraminana, 218. <https://arxiv.org/abs/astro-ph/9810074>
- Onus, A., Krumholz, M. R., & Federrath, C. 2018, *MNRAS*, 479, 1702, doi: [10.1093/mnras/sty1662](https://doi.org/10.1093/mnras/sty1662)
- Ostriker, E. C., & Shetty, R. 2011, *ApJ*, 731, 41, doi: [10.1088/0004-637X/731/1/41](https://doi.org/10.1088/0004-637X/731/1/41)
- Padoan, P., Haugbølle, T., Nordlund, Å., & Frimann, S. 2017, *ApJ*, 840, 48, doi: [10.3847/1538-4357/aa6afa](https://doi.org/10.3847/1538-4357/aa6afa)
- Padoan, P., Jones, B. J. T., & Nordlund, Å. P. 1997, *ApJ*, 474, 730, doi: [10.1086/303482](https://doi.org/10.1086/303482)
- Padoan, P., & Nordlund, Å. 2011, *ApJ*, 730, 40, doi: [10.1088/0004-637X/730/1/40](https://doi.org/10.1088/0004-637X/730/1/40)
- Pineda, J. L., Langer, W. D., Velusamy, T., & Goldsmith, P. F. 2013, *A&A*, 554, A103, doi: [10.1051/0004-6361/201321188](https://doi.org/10.1051/0004-6361/201321188)
- Radford, S. J. E., Solomon, P. M., & Downes, D. 1991, *ApJL*, 368, L15, doi: [10.1086/185937](https://doi.org/10.1086/185937)
- Rieke, G. H., Alonso-Herrero, A., Weiner, B. J., et al. 2009, *ApJ*, 692, 556, doi: [10.1088/0004-637X/692/1/556](https://doi.org/10.1088/0004-637X/692/1/556)
- Rosolowsky, E., & Leroy, A. 2006, *PASP*, 118, 590, doi: [10.1086/502982](https://doi.org/10.1086/502982)
- Salak, D., Nakai, N., Seta, M., & Miyamoto, Y. 2019, *ApJ*, 887, 143, doi: [10.3847/1538-4357/ab55dc](https://doi.org/10.3847/1538-4357/ab55dc)
- Scalo, J., Vázquez-Semadeni, E., Chappell, D., & Passot, T. 1998, *ApJ*, 504, 835, doi: [10.1086/306099](https://doi.org/10.1086/306099)
- Schneider, N., André, P., Könyves, V., et al. 2013, *ApJL*, 766, L17, doi: [10.1088/2041-8205/766/2/L17](https://doi.org/10.1088/2041-8205/766/2/L17)
- Schneider, N., Csengeri, T., Klessen, R. S., et al. 2015, *A&A*, 578, A29, doi: [10.1051/0004-6361/201424375](https://doi.org/10.1051/0004-6361/201424375)
- Schneider, N., Bontemps, S., Motte, F., et al. 2016, *A&A*, 587, A74, doi: [10.1051/0004-6361/201527144](https://doi.org/10.1051/0004-6361/201527144)
- Semenov, V. A., Kravtsov, A. V., & Gnedin, N. Y. 2017, *ApJ*, 845, 133, doi: [10.3847/1538-4357/aa8096](https://doi.org/10.3847/1538-4357/aa8096)
- Shirley, Y. L. 2015, *PASP*, 127, 299, doi: [10.1086/680342](https://doi.org/10.1086/680342)
- Sun, J., Leroy, A. K., Schrubba, A., et al. 2018, *ApJ*, 860, 172, doi: [10.3847/1538-4357/aac326](https://doi.org/10.3847/1538-4357/aac326)
- Sun, J., Leroy, A. K., Ostriker, E. C., et al. 2020, *ApJ*, 892, 148, doi: [10.3847/1538-4357/ab781c](https://doi.org/10.3847/1538-4357/ab781c)
- Tabatabaei, F. S., Krause, M., Fletcher, A., & Beck, R. 2008, *A&A*, 490, 1005, doi: [10.1051/0004-6361:200810590](https://doi.org/10.1051/0004-6361:200810590)
- Tilanus, R. P. J., & Allen, R. J. 1993, *A&A*, 274, 707
- Usero, A., Leroy, A. K., Walter, F., et al. 2015, *AJ*, 150, 115, doi: [10.1088/0004-6256/150/4/115](https://doi.org/10.1088/0004-6256/150/4/115)
- Vázquez-Semadeni, E. 1994, *ApJ*, 423, 681, doi: [10.1086/173847](https://doi.org/10.1086/173847)
- Wada, K., & Norman, C. A. 2001, *ApJ*, 547, 172, doi: [10.1086/318344](https://doi.org/10.1086/318344)
- Walker, D. L., Longmore, S. N., Zhang, Q., et al. 2018, *MNRAS*, 474, 2373, doi: [10.1093/mnras/stx2898](https://doi.org/10.1093/mnras/stx2898)
- Wilson, C. D., Bemis, A. R., & Kimli, O. submitted, *MNRAS*
- Wilson, C. D., Elmegreen, B. G., Bemis, A., & Brunetti, N. 2019, *ApJ*, 882, 5, doi: [10.3847/1538-4357/ab31f3](https://doi.org/10.3847/1538-4357/ab31f3)
- Wolfire, M. G., Hollenbach, D., & McKee, C. F. 2010, *ApJ*, 716, 1191, doi: [10.1088/0004-637X/716/2/1191](https://doi.org/10.1088/0004-637X/716/2/1191)
- Wu, J., Evans, Neal J., I., Gao, Y., et al. 2005, *ApJL*, 635, L173, doi: [10.1086/499623](https://doi.org/10.1086/499623)
- Zamora-Avilés, M., & Vázquez-Semadeni, E. 2014, *ApJ*, 793, 84, doi: [10.1088/0004-637X/793/2/84](https://doi.org/10.1088/0004-637X/793/2/84)